

**BALLISTIC TRANSPORT IN HEXAGONAL BORON  
NITRIDE/EPIGRAPHENE/SILICON CARBIDE  
HETEROSTRUCTURES**

A Dissertation  
Presented to  
The Academic Faculty

by

Grant Nunn

In Partial Fulfillment  
of the Requirements for the Degree  
Doctor of Philosophy in the  
School of Physics

Georgia Institute of Technology

August 2025

Copyright © Grant Nunn 2025

**BALLISTIC TRANSPORT IN HEXAGONAL BORON  
NITRIDE/EPIGRAPHENE/SILICON CARBIDE  
HETEROSTRUCTURES**

Approved by:

Dr. Claire Berger, Advisor  
School of Physics  
*Georgia Institute of Technology*

Dr. Zhigang Jiang  
School of Physics  
*Georgia Institute of Technology*

Dr. Walt De Heer, Advisor  
School of Physics  
*Georgia Institute of Technology*

Dr. Martin Mourigal  
School of Physics  
*Georgia Institute of Technology*

Dr. Phillip N. First  
School of Physics  
*Georgia Institute of Technology*

Dr. John Hankinson  
*Georgia Technical Research Institute*

Date Approved: May 12<sup>th</sup>, 2025

## DEDICATION

**-- To the unquenchable thirst for wonder --**

*that leads us to truth*

*like a desert wanderer chasing a mirage*

*the closer we step the more it dissolves*

*leaving only the thirst to guide us forward*

*the more we find, the more we slip*

*the harder we grasp, the more it slips away*

*yet here we walk-*

*while others turn back*

*unwilling to follow a road with no end*

**...Well then...**

*Let this be for the stubborn*

*The fools the relentless*

*the ones who keep walking*

## ACKNOWLEDGEMENTS

I extend my most heartfelt thanks to all those who have played a role in completing my thesis. My journey would not have been possible without all the support and contributions of so many people. Here is but a modest list of everyone who made this possible and but a sliver of the help they provided.

First and foremost, I thank my advisors, Claire Berger and Walt de Heer, whose guidance and leadership were instrumental in shaping the direction of my research. Claire was invaluable at working with me throughout my research. Providing suggestions for experiments and writing funding proposals was invaluable to my research. Claire provided unwavering support and offered crucial insights that greatly enriched my work. Her collaboration was a key factor in overcoming research obstacles, especially helping during challenging times like the pandemic.

Walt provided me expertise in ballistic transport and I am so grateful with his analysis of my sample displaying the edge state. Grilling me to prepare me for my thesis defense was helpful as well as finding out where I lacked knowledge and what I needed to review.

I would like to thank Vladimir Prudkovskiy: For starting me on the EG under hBN technique and training me on the BN RF sputterer as well as help via e-mail diagnosing problems.

I would like to thank Abihishek Juyal for helping extend the annealing technique to another system and providing key insights into EBSD analysis.

I would like to thank Yue Hu and Yiran Hu for introducing me to the Epigraphene lab and training me on all of the techniques.

I would like to thank current grad students Will Griffith and Noel Dudeck for helping me on various tasks in the lab. Will was invaluable at rethreading the wire-bonder and I think I would still be trying to thread that stupid wire if he didn't come help me so many times.

And thanks to Noel Dudeck for giving me a fresh perspective on my writing and presentations when I needed it. As well as for letting me steal the USB-C to HDMI adapter so many times. Why was mine always broken? (I googled why just now, I now understand why, haha)

I couldn't have done any of this without the help of so many undergrads, Fiza Shaikh doing great Raman work and helping make BN samples, Lin Beck for helping me learn new ways to automate Raman spectra capture, Han(Zhihan) Wei for doing so much work on BN and helping fix the sputterer and Marygrace Fagan for doing the initial PTCDA investigation,

I would like to thank our collaborators in TICNN including Lei Ma and others for their expertise in non-polar face samples and helping supply these invaluable chips to us. I can't wait for BN/EG/non-polar face SiC to be tried.

I would like to thank the IEN staff including Walter Henderson, David Tavakoli, and Tran-Vinh Nguyen for their expertise in characterization of thin films and training me on devices.

I would like to thank my committee members, I would like to thank Phil First for mentoring me during the Special Problems, for lending me your expertise on LEED, and for fun chatting about our electric cars. I would like to thank Zhigang Jiang for your questions about the Raman machine in our lab that left me in a 2 day literature frenzy...you might not even remember that! I would like to thank Martin Mourigal for allowing me to use/access with students the dilution refrigerator, the X-ray diffraction, and glass blowing. And I would like to thank John Hankinson for his questions at the defense and for agreeing to be a part of my committee.

I would like to thank Ed Greco for helping me through the thesis process and graduation requirements. As well as the fun times in my second and third years grading finals in person!

I would like to thank the Physics school staff including Gary Longstreet for being so supportive in the hallways and always rooting for us.

I would like to thank my grandfather Bob Prater for helping instill a thirst for knowledge and research. Truly, reading science illustrated as a kid was so motivating for the future.

I would like to thank my grandmother, Monte Prater, for reading over my manuscript, and helping me go over my defense twice. That was very helpful, but what was perhaps more helpful was being able to shoot the s\*\*t with her during breaks while I was writing my thesis.

To my parents, Tom and Deanne Nunn, thank you for supporting me especially this past year. It was extremely helpful to have such supportive parents during this time.

I would like to thank Jana Pomerantz for providing graphic design suggestions, especially for my PowerPoint and for late night cram sessions while I finished my PhD. You are invaluable.

I would like to thank the Georgia Tech Swing Dance Association, GTDA, for helping provide a fun outlet during the school year and as an ADHD way to productively use my time. Dancing does the brain wonders.

I would like to thank all those who I haven't thanked and provide another thanks to Claire. She didn't have to help me as much as she did, and I am eternally grateful for her support that exceeded my expectation.

And to all these individuals— mentioned and unmentioned—advisors, grad students, post docs, undergrad students, administrators, research experts, collaborators, industry professionals, friends, and family—I extend my sincere thanks for everyone's crucial roles in the success of my thesis. Your contributions have left an indelible mark on my academic journey, and I am deeply appreciative of each and every one of you.

# TABLE OF CONTENTS

<b>ACKNOWLEDGEMENTS</b>	<b>iv</b>
<b>LIST OF FIGURES</b>	<b>x</b>
<b>LIST OF SYMBOLS AND ABBREVIATIONS</b>	<b>xii</b>
<b>SUMMARY</b>	<b>xiii</b>
<b>CHAPTER 1. Introduction</b>	<b>1</b>
<b>1.1 Motivation</b>	<b>1</b>
1.1.1 Drude Model	2
1.1.2 Landauer Equation	3
1.1.3 Ballistic Transport in Graphene	5
1.1.4 Ballistic Transport on Graphene Hall Bars	8
<b>1.2 Graphene</b>	<b>10</b>
1.2.1 Graphene Properties	12
1.2.2 Graphene Band Structure	14
1.2.3 Graphene Production Methods	15
<b>1.3 Why Epigraphene</b>	<b>16</b>
<b>1.4 The Heterostructure Materials</b>	<b>16</b>
1.4.1 Epigraphene on SiC	18
<b>1.5 hBN Graphene Heterostructures</b>	<b>20</b>
<b>1.6 Thesis Outline</b>	<b>23</b>
<b>CHAPTER 2. Experimental Methods</b>	<b>24</b>
<b>2.1 Cleaning of SiC</b>	<b>24</b>
<b>2.2 Optical Characterization</b>	<b>25</b>
<b>2.3 Polymer-Assisted Growth</b>	<b>26</b>
<b>2.4 BN Sputtering</b>	<b>28</b>
<b>2.5 hBN Annealing</b>	<b>29</b>
<b>2.6 Characterization Methods</b>	<b>32</b>
2.6.1 Atomic Force Microscopy	32
2.6.2 Raman Spectroscopy	34
2.6.3 Cross Sectional TEM	35
2.6.4 Low Energy Electron Diffraction	36
2.6.5 X-Ray Diffraction	36
2.6.6 X-Ray Photoelectron Spectroscopy	37
<b>2.7 Fabrication Methods</b>	<b>38</b>
2.7.1 Electron Beam Evaporation	38
2.7.2 Reactive Ion Etching	40
2.7.3 Atomic Layer Deposition	41
2.7.4 PTCDA Deposition	41

<b>2.8</b>	<b>Low Temperature Transport</b>	<b>43</b>
2.8.1	Dip Stick	45
2.8.2	Cryostat	46
2.8.3	Lock-ins and Measurement	47
<b>CHAPTER 3.</b>	<b>BN/EG/SiC Device Fabrication</b>	<b>49</b>
<b>3.1</b>	<b>Heterostructure Preparation</b>	<b>49</b>
3.1.1	BN Anchoring	49
3.1.2	SiO	51
<b>3.2</b>	<b>Heterostructure Characterization</b>	<b>52</b>
3.2.1	BN Raman	52
3.2.2	XRD and XPS	53
3.2.3	BN Cross-Sectional TEM	54
3.2.4	EBSD	55
<b>3.3</b>	<b>Device Fabrication</b>	<b>56</b>
3.3.1	Charging Issue	56
3.3.2	EG Contacts	57
3.3.3	O <sub>2</sub> RIE w/hBN mask +Pd/Au	57
3.3.4	SF <sub>6</sub> +O <sub>2</sub> RIE w/MaN mask +Pd/Au	58
3.3.5	ICP etch and Pd/Au	59
3.3.6	Why Do Side Contacts Work in Other Systems?	60
3.3.7	SF <sub>6</sub> RIE	61
3.3.8	EG to FLG	62
<b>CHAPTER 4.</b>	<b>Towards Large mean free path</b>	<b>63</b>
<b>4.1</b>	<b>Hall Bar</b>	<b>63</b>
<b>4.2</b>	<b>Low Temperature Transport</b>	<b>64</b>
<b>CHAPTER 5.</b>	<b>Conclusion</b>	<b>73</b>
<b>REFERENCES</b>		<b>76</b>

## LIST OF FIGURES

	fig 1	Diagrams showing a combination of diffusive and ballistic conductors. ....	4
	fig 2	Graphene on the (2207)facet of SiC.....	6
	fig 3	4-point sidewall graphene nanoribbon measurement .....	7
	fig 4	$R4p$ showing convergence to $R0$ at 0 length.....	7
	fig 5	Band diagram showing the flat band of the edge state. ....	9
	fig 6	Graphene from history .....	11
	fig 7	Table of thickness of thin layers of graphene created from graphite oxide reduction seen in 1961 .....	12
	fig 8	Graphene lattice and band structure.....	13
	fig 9	Representation of four of the most common SiC polytypes 3C, 6H, and 4H, .....	17
	fig 10	SiC Sublimation growth schematic.....	18
	fig 11	CCS graphite crucible.....	19
	fig 12	Real space and Fourier transforms of Moiré patterns.....	22
	fig 13	Process for polymer growth.....	27
	fig 14	where $\Theta$ is the miscut angle for low miscut angle and high miscut angle[94]. .....	27
	fig 15	Pressure vs Temperature crystal phase diagram for BN.....	30
	fig 16	Cartoon of different types of pleating and their heights. ....	31
	fig 17	Cartoon of an AFM line scan for a scratch test. ....	34
	fig 18	Table showing different measured etch rates in our RIE machine. ....	41
	fig 19	PTCDA Raman signal on Epigraphene and SiC.....	42
	fig 20	Schematic of Hall bar measurement .....	43
	fig 21	Block Diagram of cryostat, .....	45
	fig 22	Block Diagram from Lake Shore Cryogenics showing a typical lock in amplifier. ....	47
	fig 23	Typical setup for measuring a Hall bar. ....	48
	fig 24	NC-AFM scan showing 6nm thick hBN square with pleating at edges. .. .....	50
	fig 25	NC-AFM scan showing 10 $\mu\text{m}$ and 20 $\mu\text{m}$ leg Hall bar hBN with pleating at edges.....	51
	fig 26	Typical Raman for various samples.....	52
	fig 27	X-ray $\theta$ -2 $\theta$ spectra for hBN .....	53
	fig 28	XPS spectra for hBN thin film.....	54
	fig 29	Preliminary results showing hBN on buffer layer on SiC. ....	54
	fig 30	EBSD results.....	55
	fig 31	Table of different methods for electrical contacts .....	57
	fig 32	Process flow for the $\text{O}_2$ RIE w/hBN mask +Pd/Au .....	58
	fig 33	Process flow for “ $\text{SF}_6+\text{O}_2$ RIE w/MaN mask +Pd/Au” and “ICP etch and Pd/Au” .....	58
	fig 34	Process Flow for $\text{SF}_6$ RIE .....	61
	fig 35	Process flow for EG to FLG contacts. ....	62

fig 36	AFM image of a typical Hall bar with 9.5 and 20 $\mu\text{m}$ legs .....	63
fig 37	Process flow for Hall bar sample.....	64
fig 38	Mobility and charge density as a function of temperature.....	65
fig 39	Resistance of 9.5 and 20 $\mu\text{m}$ legs .....	67
fig 40	Square resistance and Hall results.....	68
fig 41	Bulk square resistance adjusted .....	71
fig 42	Edge state conductance .....	71
fig 43	Edge state results.....	72
fig 44	Potential Devices .....	75

## LIST OF SYMBOLS AND ABBREVIATIONS

SiC	Silicon carbide
CCS	Confinement Controlled Sublimation
BN	Boron nitride
hBN	Hexagonal Boron nitride
EG	Epigraphene
FLG	Few Layer Graphene
EBSD	Electron Backscatter Diffraction
LEED	Low Energy Electron Diffraction
BNC	Bayonet Neill–Concelman
AFM	Atomic Force Microscopy
EFM	Electrostatic Force Microscopy
SEM	Scanning Electron Microscopy or Microscope
ARPES	Angle-Resolved Photoemission Spectroscopy
STM	Scanning Tunneling Microscopy
EDX	Energy Dispersive X-Ray (analysis/spectroscopy)
R <sub>4p</sub>	4-point Resistance
R <sub>2p</sub>	2-point Resistance
CNP	Charge Neutrality Point
ZZ	Zigzag (type of graphene edge)
AC	Armchair (type of graphene edge)
FWHM	Full Width at Half Maximum
ICP	Inductively Coupled Plasma
RIE	Reactive Ion Etching
EBSD	Electron Backscatter Diffraction
TEM	Transmission Electron Microscopy

## SUMMARY

Ballistic transport was observed in a novel hBN/epigraphene/SiC heterostructure. Such structures are of interest as graphene requires a dielectric coating for gating and protection in any optoelectronic graphene-based device architecture. I will present a new method to grow graphene fully encapsulated at the interface between a SiC substrate and a deposited BN film, ensuring that the graphene is never exposed to the environment. The technique utilizes the epigraphene growth mechanism through decomposition of the SiC interface under the BN film capping. During this process, BN crystallizes into h-BN, forming a monolithic heterostructure suitable for top-gating. I will discuss the electrical connections of epigraphene devices to external leads, with or without seamless graphene interconnects. The measured charge density is typical for epigraphene, however remarkably, significant ballistic transport is observed with a mean free path exceeding the device scale.

# CHAPTER 1. INTRODUCTION

## 1.1 Motivation

Condensed matter physics explores how the collective behavior of particles gives rise to emergent phenomena, particularly as systems are confined to lower dimensions. At reduced scales, finite-size effects dominate—surface and edge contributions become significant, altering material properties in profound ways [1-7]. One reason, these properties appear is there are more atoms that are at the edge of the material, so the edge to bulk ratio is higher, such as in nanoparticles [8]. One could define the edge as the atoms whose bonds are terminated differently than the bulk. For instance, SiC has a variety of Si-C bonds; However, at the surface of the Si side, Si-O bonds form. This 2-D sheet of SiO forms the edge of this 3-D material. If we scale down to 2-D materials such as Graphene, the edges can be Oxygen terminated forming C-O bonds. This 1-D line becomes the edge. In some other cases, confinement of electrons also contributes to emergent properties [9, 10]. Narrowing the width of a material restricts the available electronic states, increasing energy level spacing [11].

One method to confine electrons is by transitioning from 3-D to 2-D systems. Graphene, a 2-D material, offers a novel way of investigating the properties of the edge. The edge of graphene, in some situations, could operate as a 1-D material [12]. In addition, graphene has a rare band structure that could enable novel electronic states [13-15].

One common issue in graphene research revolves around the treatment of the edge and interaction with the environment [16-20]. In this thesis, we will present evidence that

covering the graphene in boron nitride (BN) using a novel technique offers a unique method of investigating the edge state by protecting the edge.

### 1.1.1 Drude Model

In 1900, Paul Drude introduced a new way to explain Ohm's law. This model considers the scattering of electrons as the explanation for resistivity and other transport properties.

It has 4 main assumptions:

- I. *Independent Electron Approximation and Free Electron Approximation:* We ignore interactions between electrons and long-range electron-nucleus interactions. Therefore, the electrons are only moved via an electro-magnetic field according to classical physics.
- II. Collisions are instantaneous events between electron and static ions. While this assumption is often good enough and what Drude did, it is not true. We can just assume there is some scattering process and keep this assumption for now.
- III. The probability of having a scattering event between a unit of time is  $1/\tau$  where the time  $\tau$  is the relaxation time, the collision time, or the mean free time. Whatever you call it, this time is the average time between collisions in the Drude model and any electron we choose will on average have had time  $\tau$  since its last collision and  $\tau$  until its next collision [21].
- IV. Electrons are in thermal equilibrium with their environment only through collisions. Where, immediately after a collision the electron is ejected with a speed appropriate with the temperature despite what its speed was before the collision.

We begin with electrons behaving like balls in a pinball machine where electrons travel between scattering centers via the Lorentz force. The scattering centers are the immobile positive ions of the solid. We can call these electron-nucleus interactions Drude scattering. There are other interactions, such as electron-electron interactions, but those are assumed to be small compared to Drude scattering. The time it takes to scatter off of these positive immobile ions is assumed to be zero as well. These immobile ions are given charge  $eZ_a$  with a surrounding charge around the atom of  $Z_a - Z$  where  $Z$  is the number of weakly bound valence electrons which contribute to conduction. From this we can derive a whole host of properties [22].

The Drude model considers an ideal metal where the scattering is exclusively at the atoms in the solid. In reality, there is scattering from phonons and crystal defects as well. Impurity scattering is independent of temperature, while phonon scattering depends on temperature. For many systems, phonon scattering may need to be minimized, so researchers go to cryogenic temperatures to reduce this effect [21].

### *1.1.2 Landauer Equation*

With the advent of quantum mechanics and the Pauli exclusion principle, it became evident that there were serious problems with the classical Drude model [21]. When we reduce the size of wires to the nm scale, we can limit the number of channels available to the electrons [11]. The Drude model has broken down because of these limited number of states. As we increase the number of states, we recover the Drude model, as expected.

The Landauer equation explains this:

$$G = 2 \frac{e^2}{h} \sum_n N T_n \quad (1)$$

Where  $N$  is the total number of channels with transmission probability  $T_n$  [21].

If the mean free path,  $\lambda$ , of a channel is much longer than the conductor length, then the resistance is  $R_0 = \frac{1}{G_0} = 25.6k\Omega$  where  $G_0 = \frac{e^2}{h}$  is the conductance quantum [21]. For any single channel ballistic conductor, the resistance tends to  $R_0$  at zero length. The energy from the resistance is deposited into the contacts as heat, while the conductor does not receive any energy from the current.

In the presence of scattering, the transmission probability for any conductor of length  $L$  goes as  $T = \frac{\lambda_N}{L + \lambda_N}$  where  $\lambda_N$  is a characteristic length or the mean free path. Note, for long conductors with many channels, we recover  $R = \frac{\rho L}{A}$  where  $A$  is the cross sectional area of the conductor and  $\rho$  is the resistivity of the material [11].

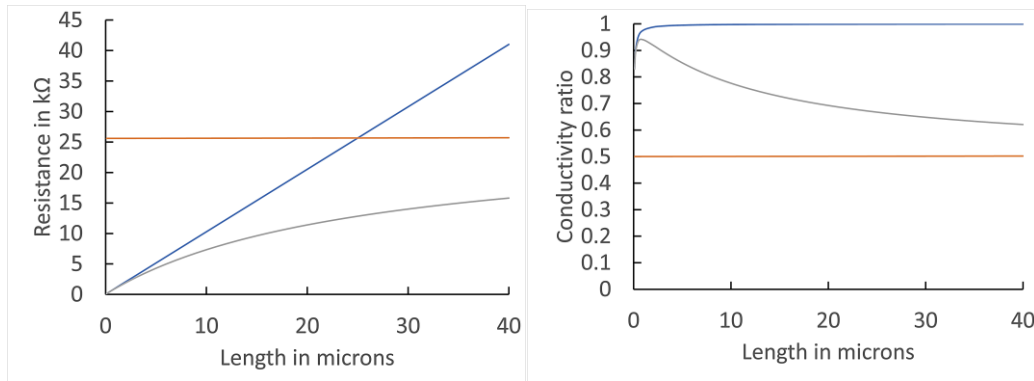


*fig 1 Diagrams showing a combination of diffusive and ballistic conductors. Left) Resistance vs length for different ballistic conductors. In orange 1 channel with a mfp of 1mm, in blue 500 channels with a mfp of 50nm. And grey shows the addition of the two. Right) Conductance of twice the length divided by the conductance from graph 1a (or, in other words,  $G(2L)/G(L)$  vs.  $L$ ). For ballistic conductors this should always be 0.5, while for ohmic conductors this should be 1 due to Ohm's law.*

We could have a system where a ballistic channel and a diffusive channel are in parallel. In such a system, the resistance will trend towards 0 ohms at 0 length; however, the resistance will scale differently with length. If we compare the conductivities of length,  $L$ , and length  $2L$ , we will notice that this conductivity ratio will not equal 1 as in a completely diffusive channel and it will not equal 0.5 as in a ballistic channel. Instead, it will be somewhere in between. In this way, there is a smoking gun for systems made out of these two channels in parallel. Now, we can talk about a system that displays such an effect, graphene.

### 1.1.3 Ballistic Transport in Graphene

Since graphene lacks a bandgap and most electronics require a bandgap for digital electronic applications, some researchers seek to open the gap [23-33]. One method is by confinement of electrons in a nanoribbon. When graphene is cut, there can be two principal edges, the armchair edge and the zigzag edge. For a graphene of width  $w$ , we can quantize the motion of electrons such that,  $k_y = n \frac{\pi}{w}$  where  $n$  is an integer. For the  $n$ th electronic subband the energy is [11].

$$E_n = \frac{\hbar^2 \pi^2}{2mL^2} n^2 \quad (2)$$

In a 2014 Nature article [15], de Heer's team at Georgia Tech reported results on etched trenches 20nm deep in the  $(1\bar{1}00)$  direction of single crystal SiC and annealed samples at 1600°C for 15mins. This forms a natural-step EG ribbon that leads can then be connected to. Samples were characterized using AFM, EFM, SEM and conducting AFM. Finally, ARPES was performed and showed a Dirac cone with an angle consistent with the

( $2\bar{2}07$ ) facet and in conjunction with STM, researchers show charge neutral graphene on the sidewalls on the zig-zag edge. Where fig 2 shows graphene grown on the sidewall of SiC.

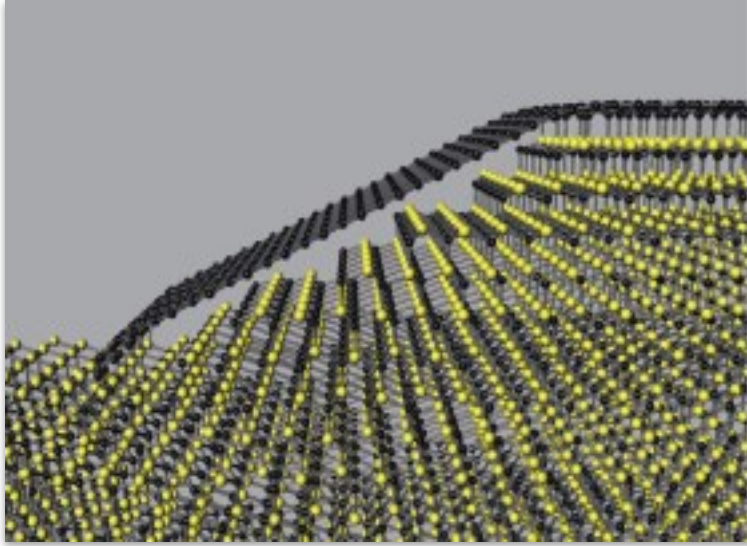


*fig 2 Graphene on the ( $2\bar{2}07$ ) facet of SiC. Carbon in black, silicon in yellow[34]*

Later, a top gate of Al on 20nm  $\text{Al}_2\text{O}_3$  was added as well as graphene leads for 4-point electron transport measurements.  $R_{4p}$  (the 4-point resistance) converges to  $R_0$  which we define in this proposal as  $h/e^2$  (not accounting for 2 spin states). This convergence to  $R_0$  is shown in fig 4. In addition,  $R_{4p}/R_{2p}$  (the 4-point resistance divided by the 2-point resistance) is close to 1 showing near perfect invasive contacts [21, 35, 36]. Later, sharp tungsten probes were used instead of graphene and in situ variable-geometry transport was performed [15]. The Omicron nanoprobe system is shown in fig 3 with the right image being an SEM image of the probes. Initially only two probes were connected to the sample. If a third probe is added between these two probes,  $R_{2p}$  changes from  $R_0$  to  $2R_0$  indicating the transmission probability is 0.5. For ballistic conduction, invasive probes cause a change in conduction just like what we see here. Side-wall ribbons show this unique edge

state, where exfoliated graphene ribbons do not because of disorder at the edge of the exfoliated and etched graphene.

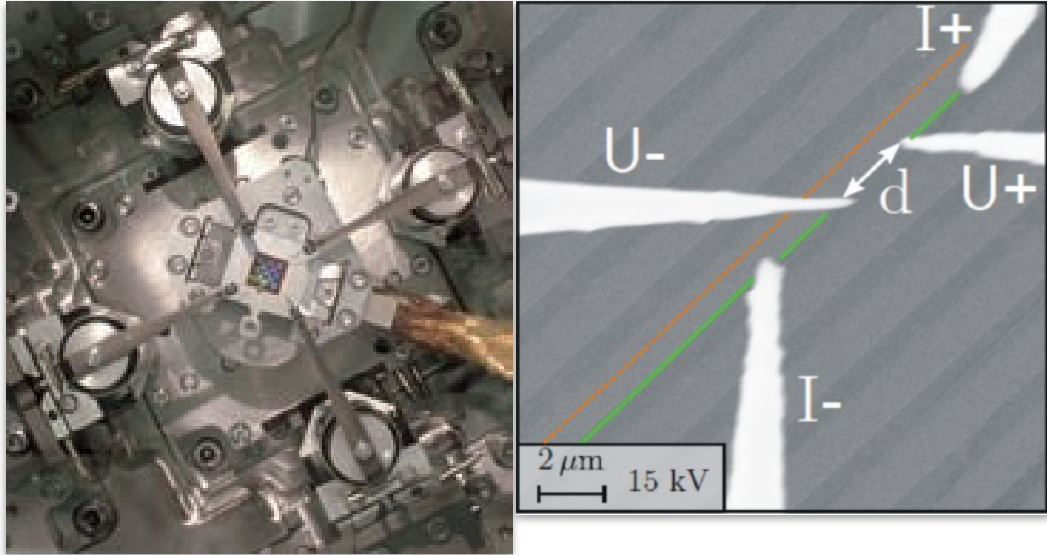


fig 3 4-point sidewall graphene nanoribbon measurement Left: The Omicron nanoprobe system showing the four probes and the sample from above. Right: A 4-point measurement being taken where current is injected from I+ to I- and voltage is measured from U+ to U-[15].

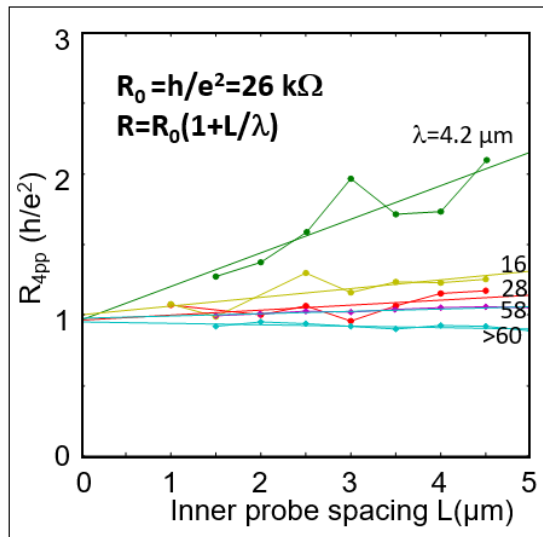


fig 4  $R_{4p}$  showing convergence to  $R_0$  at 0 length[15].

#### 1.1.4 Ballistic Transport on Graphene Hall Bars

Samples on the  $\bar{1}105$  face (a non-polar face) on 4H SiC were grown using Confinement Controlled Sublimation (CCS) method and Hall bars were created with an alumina gate. During processing, the etched edge does not have a well-defined chirality and is not necessarily straight. ARPES shows charge neutral graphene and Raman shows a small D peak with a 2D FWHM of  $28.8\text{cm}^{-1}$ . In de Heer's team, it was found that an edge state is created via two methods [37]. Using ICP etching, high energy ions cause high local temperatures which fuse the EG edges to the SiC. Via cross-sectional electron microscopy [38], these acene edge atoms are believed to be bonded to the substrate with a single unoccupied state at  $E=0$ . The large density of states pins the Fermi level at the edge to  $E=0$ . Another method of bonding the edge to the substrate involves RIE etching the graphene then annealing at high temperature to remove the C-O bonds allowing relaxation bonding to the substrate.

The conductance was measured vs. gate voltage and at CNP the conductance reaches a minimum but does not vanish. The point being, as the calculated diffusive part of conduction is removed the single state at the Dirac point remains. This is easily explained by the Landauer equation [21].

$$G = \sum G_0 \left(1 + \frac{L}{\lambda_N}\right)^{-1} \quad (3)$$

Where  $\lambda_N$  is the mean free path of each path; however, for  $\lambda_N \ll L$  with only one ballistic channel you obtain:

$$G = G_{ballistic} + G_{diffusive} = G_0 \left( 1 + \frac{L}{\lambda_{ballistic}} \right)^{-1} + \frac{\sigma W}{L} \quad (4)$$

Where at CNP, sigma goes to 0, we are left with only the ballistic contribution, which turns out to be localized to the edge. Solving for  $\lambda$  we found experimentally  $\lambda_{ZZ} > 50 \mu m$  and  $\lambda_{AC} = 5 \mu m$ . And plugging in the diffusive part, we find  $\lambda_{diffusive} \sim 10nm$  [34].

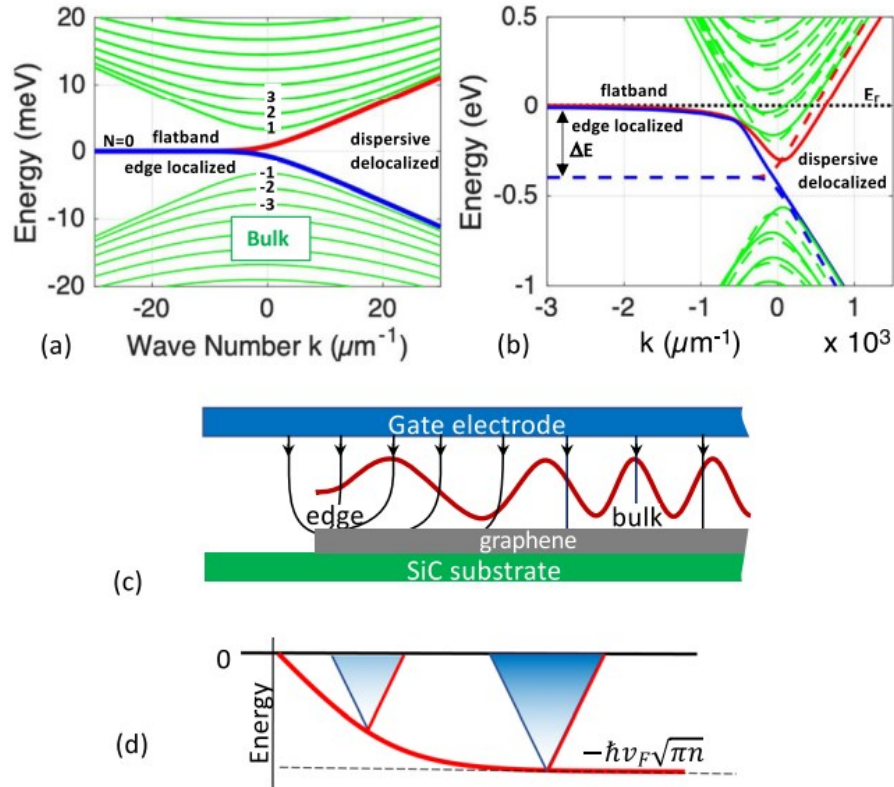


fig 5 Band diagram showing the flat band of the edge state. a) At 0 Fermi energy b) At a Fermi energy above the band gap of the diffusive contribution. c) field lines for a gate. d) Fermi energy as a function of distance from edge. [34]

At CNP, voltage measurements on opposing sides of the Hall bar lineup exactly with magnetic field showing both sides of the Hall bar contribute equally to electron transport. Furthermore, at high magnetic fields, conductance of edges scale with the number of junctions that function as scattering centers adding  $1 R_0$  per junction. This has been seen in the armchair and zigzag directions. These samples also had no Hall voltage despite current flowing through the sample. This means electron and holes are contributing to the conduction at the edge state. Furthermore, as temperature increases a second ballistic state begins to conduct with an energy 10meV above the Fermi level. This is believed to be spin splitting of the edge state, which lifts the spin degeneracy. This suggests that electron-hole pairs are traveling at the edge in a state that is a spin  $\frac{1}{2}$  Fermion [34], perhaps similar to that proposed by Majorana [39-42].

This effect is created via the unique band structure of this system. The graphene edge is composed of an edge localized flat band pinned at zero energy combining with two hyperbolic delocalized linearly dispersive bands, while the hyperbolic sub-bands exist in the bulk. This edge state is not only isolated in space. It is isolated in energy as well. Due to this separation, the ballistic channels and the diffusive channels do not mix [15].

## **1.2 Graphene**

The 2010 Nobel Prize brought much interest to graphene, but the story of graphene can be traced back to the to the 19<sup>th</sup> century.

We go back to Benjamin Brodie in 1859 where he exposed graphite to strong acids the resulting mixture he called “carbonic acid” which can be seen in fig 6a. While he believed

he had made a new form of carbon he called “graphon”, he had actually made a suspension of graphene oxide [43].

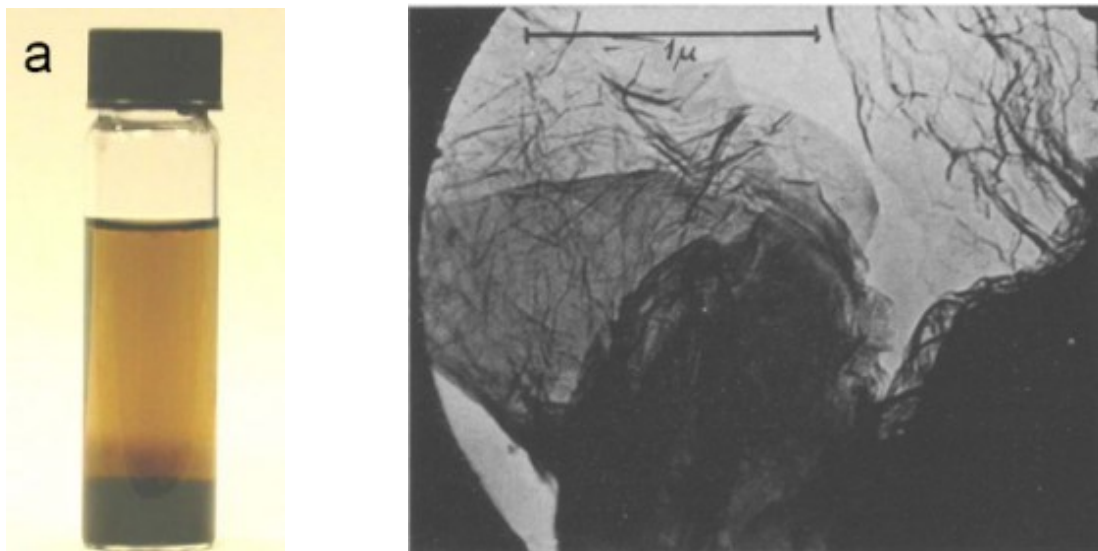


*fig 6 Graphene from history a. Recreation of graphene seen by Brodie in 1859. Graphite oxide is at the bottom which dissolves into graphene forming a yellow/orange suspension of graphene flakes. [44, 45] b. Electron microscope image of a graphene oxide suspension showing creases/pleats indicative of a 2-D material [46].*

Skipping to 1948 Ruess and Vogt performed TEM on a droplet of graphene oxide suspension where they saw creased flakes at a few nm in thickness.[46] The electron microscopy image of these results can be seen in fig 6b. This research continued when in 1961 (some manuscripts say 1962) Ulrich Hofmann and Hanns-Peter Boehm identified thin films with integer level spacing, clearly showing single layer “graphitic lamellae”[47] TEM will be discussed in Chapter 2.

The thickness of graphene can be easily measured today using STM, AFM, or TEM. That being said, although it is claimed that the methods used by Ruess and Vogt would not stand up to modern scrutiny[44], Ruess and Vogt measured an average of 4.6 Angstroms

while graphene on SiO<sub>2</sub> has a thickness of 3.5 Angstroms. In fig 7 you can see the original table showing the quantization of thickness, a clear sign they achieved single atom thickness.

**TABLE III**  
*Thicknesses of Extremely Thin Carbon Lamellae*

3.0 Å	7.6 Å	12.4 Å	16.7 Å	22.8 Å
3.3	8.3	12.4	19.9	23.6
3.3	8.7	12.6		
3.8	9.1	13.1		
3.9	9.2	13.5		
4.0	9.8	13.9		
4.5	10.9	14.6		
4.5	11.5	15.1		
4.6		15.3		
4.6				
4.9				
5.2				
6.0				
6.1				
6.1				
6.3				
<b>Average:</b> 4.6 Å	9.5 Å	13.7 Å	18.3 Å	23.2 Å

*fig 7 Table of thickness of thin layers of graphene created from graphite oxide reduction seen in 1961[48]*

### 1.2.1 Graphene Properties

Graphene consists of carbon atoms arranged in a honeycomb lattice consisting of sp<sup>2</sup> hybridized atoms. We may define such a lattice by defining a basis of two atoms in a unit cell with a triangular lattice, where any two neighboring atoms are separated by a length  $a = 0.142\text{nm}$ . We can then obtain the reciprocal lattice space from this definition. In the first Brillouin zones, there exist points K and K' where near the K and K' points we can approximate with a linear dispersion relation. The lattice, reciprocal lattice, and band structure are shown in fig 8. At these points the valence band and conduction band touch

each other at zero energy, a point called the Dirac point. This linear dispersion relation shows that near the Dirac point the Fermi velocity is constant just like zero mass photons. Because of this property, we see properties such as the anomalous quantum Hall effect, plateaus in the Hall resistance that show a Berry phase of  $\pi$ . There are two orientations we can cut graphene in such that if we cut in the  $a_1+a_2$  direction we have an edge that we call an armchair edge direction (horizontal in fig 1); if we cut in the  $a_1-a_2$  direction we have a zigzag edge direction (vertical in fig 1)[49]. Finally, there are various structures made up of graphene such as carbon nanotubes which were studied in this lab previously[50].

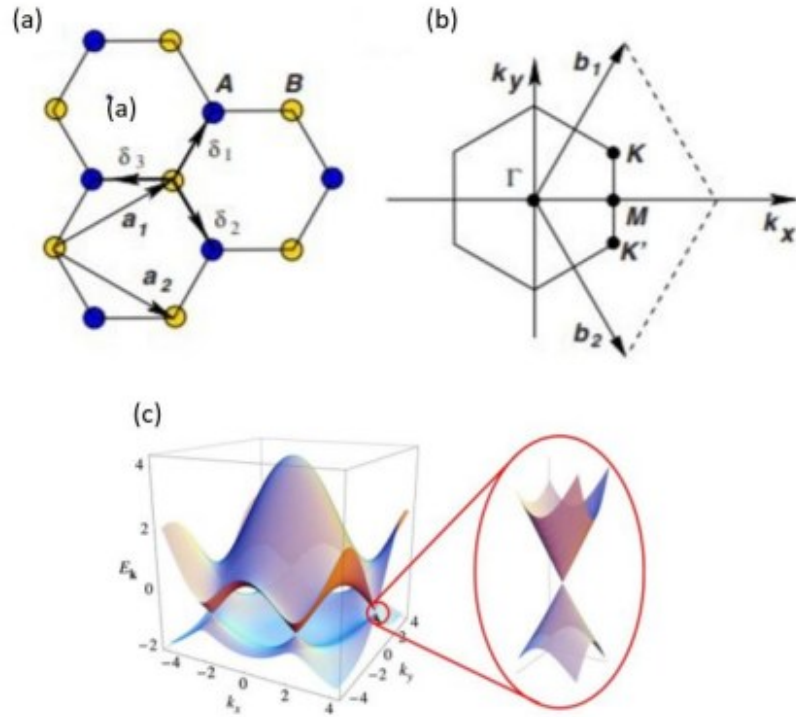


*fig 8 Graphene lattice and band structure (a) graphene lattice structure showing A and B atoms in the Basis and lattice vectors  $a_1$  and  $a_2$  (b) Reciprocal space and the first Brillouin zone. Dirac points located at points  $k$  and  $K'$ . (c) tight binding calculation of the band structure showing the linear dispersion relation at the Dirac point[9].*

$$\vec{a}_1 = \frac{a}{2}(3, \sqrt{3}), \vec{a}_2 = \frac{a}{2}(3, -\sqrt{3}) \quad (5)$$

$$\vec{b}_1 = \frac{2\pi}{2a}(1, \sqrt{3}), \vec{b}_2 = \frac{2\pi}{2a}(1, -\sqrt{3}) \quad (6)$$

### 1.2.2 Graphene Band Structure

We can write the Hamiltonian of graphene and include the 3 nearest neighbors, tight binding approximation.

$$H(R) = -t \sum_R [|R\rangle\langle R+b| + |R\rangle\langle R+b+a_1| + |R\rangle\langle R+b+a_2|] \quad (7)$$

Where  $R$  is the state at position  $R$  of the first atom in the lattice and  $b$  is the direction to the second atom in the basis [13]. The eigenenergies of this Hamiltonian can be solved for:

$$|E(\mathbf{k})| = t \sqrt{1 + 4 \cos^2 \frac{k_y a}{2} + 4 \cos \frac{\sqrt{3} k_x a}{2} \cos \frac{k_y a}{2}} \quad (8)$$

Where  $k_x$  and  $k_y$  are components of the reciprocal lattice and  $t$  is the hopping integral  $\sim 2.7\text{eV}$ [49]. Expanding around the K points we find

$$E \cong \hbar v_f k \quad (9)$$

Where  $v_f$  represents the Fermi velocity[13]. Now that we know the properties of graphene and why it is of interest we can talk about different production methods for graphene.

### *1.2.3 Graphene Production Methods*

Graphene can be produced in a variety of ways for electronic research applications. Exfoliation via scotch tape is one example [51]; however, more sophisticated methods exist. Exfoliation via sonication of suspended graphite followed by a jaunt to the centrifuge yields multilayer graphene flakes that are oriented in random directions. There are also various other transfer methods using polymers to help hold the graphene together during the transfer process [1]. For many applications that seek to exploit the mechanical properties of graphene, micrometre sized flakes may be enough, but for electronic applications where crystal orientation, cleanliness, reproducibility, and wafer-scalability matter, these methods may not be an ideal solution [52].

Chemical Vapor Deposition (CVD) [27, 53], growth is another method of producing graphene. In CVD growth, a carbon-containing molecule such as methane is pumped into a chamber onto a reactive surface leaving carbon that reorganizes into graphene on the surface. The resulting graphene can then be transferred to a useful substrate such as Si, SiO<sub>2</sub> or SiC.

Another form of graphene of interest is graphite oxide (GO) [54]. GO can be used in a variety of applications. Of note it is used as a component of Lithium-ion battery(cathodes). GO and graphene resist plating compared to their graphite counterparts [55] [54]. We have been interested in GO because it can be reduced to produce graphene.

GO is commonly produced using the Hummer method which consists of treating graphite with sulfuric acid, sodium nitrate, and potassium permanganate in that order [54]. This was studied previously in this lab [56].

### **1.3 Why Epigraphene**

The key difference is that this lab works on epigraphene (graphene grown epitaxially on silicon carbide) exclusively. Furthermore, this lab has seen the edge state with a fair amount of consistency; however, other labs do not see this ballistic edge state. The key difference is that this lab works on epigraphene exclusively. This makes the graphene edges unique [57-63]. Graphene edges in other systems are exposed to the environment and are oxygen terminated [9, 64, 65]. Epigraphene edges can be terminated in oxygen or terminated into the SiC. We can anchor the graphene to the SiC by annealing at high temperatures, 1200°C, or by using dry etching techniques which effectively weld the graphene to the SiC. These methods pin the edge state to zero energy, which preserves the flat band at the edge of graphene. In addition, SiC is commercially available, relatively cheap, and compatible with conventional electronic fabrication methods [13, 66]. Now we'll discuss SiC and hBN which will support our investigation of the edge state and sandwich our graphene.

### **1.4 The Heterostructure Materials**

SiC comes in a variety of different polytypes [67]. Four common ones are 3C, 4H, 6H, and 15R. The number corresponds to the number of SiC bilayers to repeat the pattern while the letters correspond to the crystal type: Cubic, Hexagonal, and Rhombohedral. A representation of the most common polytypes is shown in fig 9. In this lab, we use



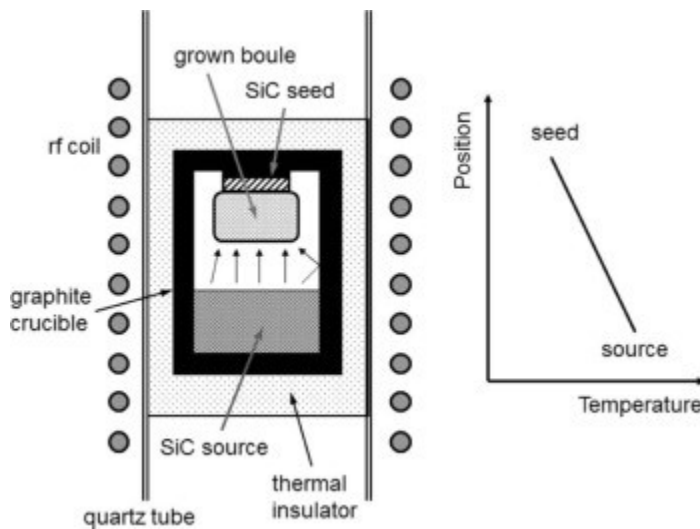


*fig 10 SiC Sublimation growth schematic[73]*

The difference in temperature creates a difference in vapor pressure that causes matter to transfer from the source to the seed in this non-equilibrium state. A schematic of this process is shown in fig 10.

This process also occurs on a smaller scale in our furnaces. As a temperature gradient is kept between the seed chip and the source chip, SiC subspecies can be deposited onto the surface. Controlling the temperature gradient will determine the rate of deposition. This method is used in our lab, but will not be expanded about in this thesis [73].

#### *1.4.1 Epigraphene on SiC*

SiC, when heated, decomposes such that a single layer of graphene can form if enough Si atoms escape the surface. This process is a function of the silicon vapor pressure at the surface of the chip. To control the growth, one may grow graphene using confinement-controlled sublimation growth (CCS)[74, 75]. CCS involves placing a SiC

chip inside a graphite crucible inside a vacuum chamber. The graphite crucible is then heated using an induction coil outside the vacuum chamber to a temperature which sublimates Si from SiC, leaving behind a single layer of carbon atoms which reorganize into the most stable crystal for the carbon which is graphene. For 6H and 4H, 3 SiC bilayers results in about one graphene layer[76]. Induction heating prevents impurities being introduced from a heating element and temperature is monitored by a pyrometer using the black body radiation from the graphite crucible. Controlling the growth rate requires tuning of the Si leak rate of the crucible, the temperature-time profile, and the crucible condition [72, 77]. A diagram of a typical CCS method and an ultra confined CCS method is shown in fig 11. When the Si sublimates, it escapes from the surface via planar diffusion across the surface and step edges[78].

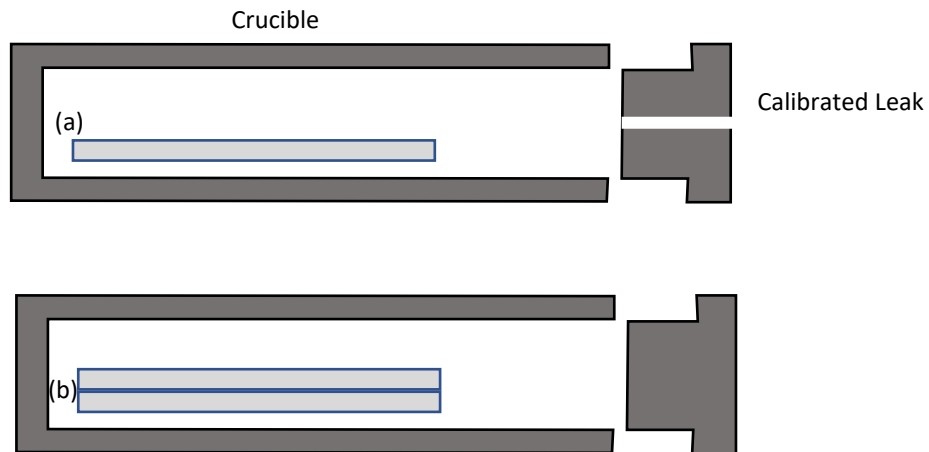


*fig 11 CCS graphite crucible(a) schematic for the graphite crucible. A cylindrical graphite crucible is constructed and placed in a vacuum chamber. (b) schematic for annealing SiC without growing graphene. Si pressure from a donor chip and Ar pressure suppresses graphene growth at high temperatures.*

Graphene on the carbon face is rotationally stacked, and the morphology shows pleating indicative of the negative thermal expansion of graphene compared to SiC; however, graphene on the Si face starts with a layer, called the buffer layer, which is strongly bonded to the SiC surface [79, 80]. The next layer is monolayer graphene and

instead of pleating like C-face graphene, the layer is strained in a way that causes a change in the Raman signature shifting the 2D peak [81]. In addition, the orientation of the buffer and graphene layer are fixed by the lattice of the SiC making the graphene epitaxial to the SiC.

EG has several interesting properties compared to idealized graphene from models. For instance, SiC has a bond length of 1.87 Angstroms, while graphene has a bond length of 1.42 Angstroms. Due to the hetero epitaxy, there is quasi match for 13 cells of EG between graphene and Si face. The buffer layer is heavily bonded to the SiC, and this bonding changes the band structure of the graphene turning it into a semiconductor, which is why we do not call this layer graphene, but rather buffer or buffer layer [80, 82]. The electronic properties of the graphene layer above the buffer layer remain unaffected; however, the graphene is doped when on the Si face. On the Si face, the buffer layer is n doped and then the next layer which is graphene is n doped but can be easily p doped by the environment [83, 84].

If we cut SiC at an angle, we get a mix of carbon and silicon at the surface of SiC. We call this class of faces “non-polar faces.” The resulting graphene is closer to charge neutral and displays faster growth [85].

## **1.5 hBN Graphene Heterostructures**

Hexagonal boron nitride (hBN) and graphene have been used in hBN/graphene heterostructures thanks in large part to the nearly identical lattice constants of hBN and graphene [86, 87]. This lab also investigated hBN and graphene previously using MOVPE;

however, RF sputtering is simpler and has the added benefit of creating environmentally protected graphene.

Boron nitride comes in a variety of different polytypes. Amorphous(a), hexagonal(h), cubic(c), and wurtzite(w) are the most common types. BN is a semiconductor, though not a great dielectric for gating. Its low frictional force coefficient in its amorphous and hexagonal form makes it a great lubricant, just like graphite. In vacuum, we find a-BN transitions to hBN above 1550°C. We can exploit this property in the creation of hBN/EG devices [87-90].

hBN is a honeycomb layered structure with similarities with graphite, that stacks in an AA' configuration with the boron and nitrogen over one another. The intralayer bonds are made up of sigma bonds, while the interlayer bonding is mostly Van der Waals interactions. This gives rise to a negative thermal expansion coefficient in the in-plane direction and a positive coefficient of thermal expansion in the out of plane direction. hBN can also be intercalated with carbon forming boron nitrogen carbon materials, which is especially important to note since we will be combining graphene and BN to make devices [91].

Reducing or eliminating substrate effects have been a goal for researchers ever since graphene was discovered. While graphene on SiO<sub>2</sub> can be identified easily via optical contrast, SiO<sub>2</sub> has its own problems as a substrate. Charge puddles in the oxide layer of Si lead to charge localization in graphene that cannot be removed by a global gate. Instead, researchers used exfoliated hBN as an interstitial layer between SiO<sub>2</sub> and graphene. This heterostructure showed Moiré patterns in the STM topography [92]. Moiré patterns of hBN on graphene are shown on fig 12.

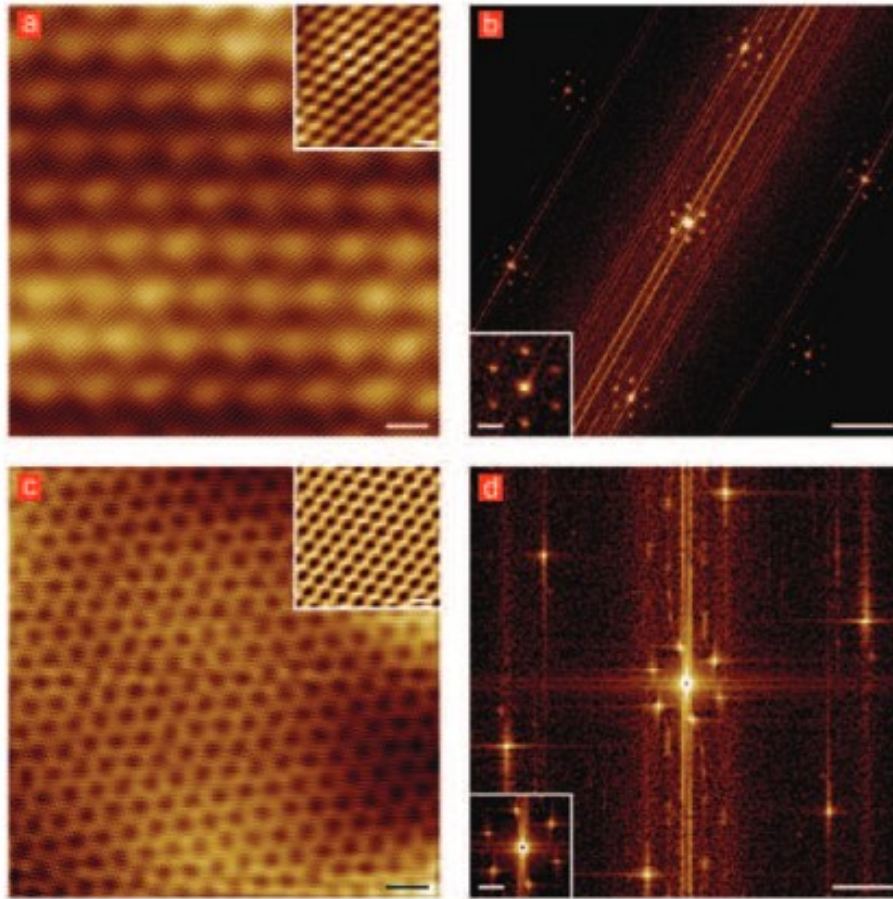


fig 12 Real space and Fourier transforms of Moiré patterns a) STM topographic images of a Moiré pattern produced by graphene on hBN with a scale bar 2 nm. The inset is a 2 nm region with a scalebar of 0.3 nm b) Fourier transform of (a) with scale bar of 10 nm<sup>-1</sup> inset is one of the lattice points with a scale bar of 2 nm<sup>-1</sup> c) Same graphene flake on hBN as (a), but in a different location showing a different Moiré pattern with a scale bar 2nm. The inset is a 2 nm region with a scalebar of 0.3 nm. b) Fourier transform of (c) with scale bar of 10 nm<sup>-1</sup> inset is one of the lattice points with a scale bar of 4 nm<sup>-1</sup>[93].

## 1.6 Thesis Outline

Past work showed a very long mfp in sidewall epigraphene nanoribbons, but it was believed that this mfp was still being degraded and reduced by environmental factors. This thesis outlines my work to protect epigraphene nanoribbons from environmental degradation using hexagon boron nitride. In chapter 2 I will discuss the experimental tools and techniques used to create my samples and the Hall bar discussed in later chapters. In chapter 3 I will discuss the characterization performed on these heterostructures and the process through which I optimized the hBN/EG devices. In chapter 4 I will present the electrical characterization I performed on an hBN/EG Hall bar that demonstrates a mfp of over 1mm,  $\lambda = 1080 \mu\text{m} \pm 228 \mu\text{m}$ . Finally in chapter 5 I will discuss the importance of these results and suggest further experiments to continue exploring the epigraphene edge state.

## CHAPTER 2. EXPERIMENTAL METHODS

In this chapter I will go over various techniques and equipment which are used later in chapter 3. I present these as ways my thesis was done. Many times, there is an alternative way to do certain tasks. In some instances, we do not have the capabilities or expertise in this lab to perform the technique. However, in most instances, it is because I am already an expert in this task and know the process completely. For instance, while I can do photolithography, I am not an expert and do not know how the different masks will affect my sample. Electron beam lithography is something I have been trained in and can do readily. Furthermore, I know how to remove the mask very well. To that end, I choose e-beam lithography rather than photolithography despite my device sizes being an ideal size for photolithography. I will later find out, perhaps the undercut caused by the secondary electrons aided my process.

### 2.1 Cleaning of SiC

SiC comes in large wafers which need to be diced for testing purposes. The dicing process we use involves putting the wafer on an adhesive and cutting with a thin diamond saw. This process requires immense patience and technique, and the Marcus Cleanroom staff graciously offers that service to us. Once we have the diced wafer we need to prep it for graphene growth, sputtering BN or whatever the process will be. First, we mark the chip by chipping one corner. Without this step we would not know the orientation of the wafer was. This is important for knowing the miscut of the chip as well as the crystal orientation.

Getting the adhesive off is the first step to the process and a necessary step. The glue will immediately burn in our furnaces and can alter our results. This removal is done with an acetone sonication, followed by removal of the adhesive with a Kimwipes and acetone followed by an acetone sonication to an IPA sonication. This whole time we must make sure to use Teflon tweezers as metal tweezers can cause the edges of the chip to crack.

If that is not enough, we can even remove all the adhesives by oxygen etching using RIE. Which brings us to our next hurdle for prepping the SiC surface. Whether we oxygen etch or just leave the SiC chip in air. The surface of the Si face will be covered in SiO<sub>2</sub> bonds. There are other methods to use, but our method is to bake the SiC chip at 1250°C for 20 minutes. This is probably overkill to remove SiO<sub>2</sub>, but graphene growth happens at even higher temperatures, so this is not a problem.

## **2.2 Optical Characterization**

Since Ruess and Vogt had difficulty in 1948 to find single layer graphene, it may come as no surprise that finding graphene would be difficult. AFM and Raman spectroscopy, while reliable, are dreadfully slow if you are looking for features. Indeed, Geim found graphene was completely invisible optically with a SiO<sub>2</sub> thickness of 300nm, which is notable because standard wafers have a thickness of 300nm; However changing the thickness to just 315nm made the graphene visible [1]. This is thanks to interference effects reflecting off the Si wafer.

All these problems we do not have to worry about, because insulating SiC is transparent to visible light. This makes finding graphene on the surface extremely easy

and quick. When using an optical microscope, we can even differentiate between areas of overgrowth such as the bilayer graphene and areas of undergrowth such as buffer layer. Combined with AFM and Raman, we can quickly categorize any patches we see.

BN is a different matter. Thin films of deposited BN are extremely difficult to see and there are no growth patches from the sputtering process. Sputtered BN is a white color and does not give as much contrast as the black of graphene. Instead, we must rely on other methods to find BN.

Once BN is annealed, it is a different story. After annealing BN on SiC pleats. These pleats are easily seen as they scatter light in other directions making them a darker shade. Differentiating thicknesses of BN is still not possible, but the presence of hBN is extremely obvious in an optical microscope.

### **2.3 Polymer-Assisted Growth**

Polymer growth was found to produce more homogenous high-quality graphene across the surface of SiC. In addition, polymer growth results in little step flow and less bilayer/buffer inclusions on the surface[37, 94]. Polymer growth works by donating carbon by carbonizing the polymer with heat. The resulting carbon then reorganizes at high temperature to form graphene without carbon contribution from SiC. In this method. SiC acts as a template for the graphene to later form. The process starts by making a mixture of 50mL of AZ and 40mL of IPA. This mixture is then quickly spin coated at 4500RPM onto the sample. This must be done quickly as AZ will quickly separate from IPA. This process results in an AZ layer that is a few nm thick with an optimum thickness of 10-15 nm. AZ is typically used as a photoresist with a minimum recommended thickness of 1

$\mu\text{m}$  where a negative profile is desired[95], but here we are just using it for its carbon contribution. Since the IPA evaporates, there is no need for a post bake to remove the IPA compared to other spin coating methods. Next the sample is annealed at  $1250^\circ\text{C}$ . In addition to removing SiO, this step removes all the O and H in the polymer leaving only C. Next, we heat up the sample even more, which sublimates a few layers of Si, and the carbonized polymer reorganizes itself into monolayer graphene. One obvious question, is does this process work with other polymers? The answer is a definitive yes. Graphene has been produced from a variety of materials from petroleum waste to manure. Since we seek monolayer graphene, we need to have the same amount of carbon per unit area in our polymer as monolayer graphene. A diagram of the PTCD A deposition process is shown in fig 13.

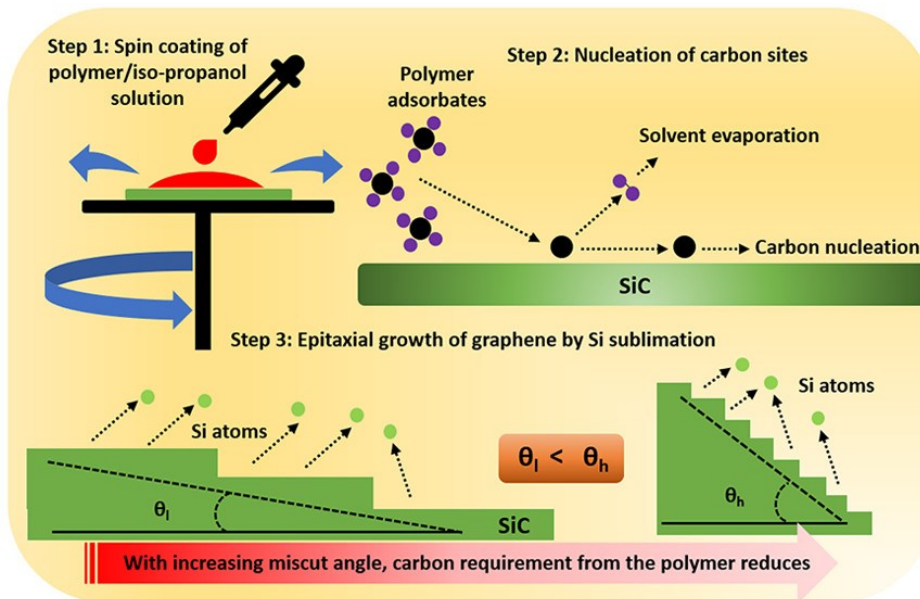


fig 13 Process for polymer growth where  $\theta$  is the miscut angle for low miscut angle and high miscut angle[94].

While this is an innovative way to grow graphene on SiC, it is not compatible with sputtering as the sputtering process destroys graphene and the polymer; however, after BN

has been annealed to hBN, this polymer becomes an excellent interstitial layer between hBN and Alumina.

## 2.4 BN Sputtering

Since BN is an insulator, RF sputtering is a standard method to deposit such an insulator. Like many thin film methods, careful care needs to be taken to make sure the BN will adhere to the SiC. To that end, the SiC chip needs to have all the Si-O bonds removed leaving a bare SiC surface for the BN to attach to. If one does not remove all the SiO, the BN will not adhere and annealing or rough handling of the sample will exfoliate the BN from the surface. There are a variety of methods to remove SiO<sub>2</sub>. This lab removes SiO<sub>2</sub> with a 1250°C anneal in vacuum for a minimum of 30 minutes. Other methods are available such as wet etching with an acid like HF or a brief dry etching of SF<sub>6</sub> or BCl<sub>3</sub>. Dry etching roughens the surface of SiC and wet etching is not in situ, so it is less desirable as the sample must be put in vacuum immediately else the SiO reforms. However, the surface is prepared, next the sample needs to be brought to 400°C and equal parts Ar and N<sub>2</sub> need to be introduced at a total pressure of  $2 \times 10^3$  mbar. This combination ensures stoichiometric BN[96]. Next, the plasma is ignited with a burst of N<sub>2</sub> at a power of 100W. In addition to the plasma, the BN target gets bombarded by electrons accelerated by the DC bias. This knocks boron and nitrogen atoms from the target, which are ionized and accelerated downwards toward the sample. The DC bias is between 220V and 300V and controlled via the RF generator.

Some complications arise from this configuration. The mounting screws made of steel and the target holder and the heating coils made of copper are also deposited onto the

sample. While this is in only tiny amounts, higher purity is needed. We have a solution. All exposed components are coated in a thin coat of BN spray such as that sold by ZYP coatings.

In addition, if you want the sample to be baked in the chamber and then immediately sputtered, the crystal monitor must be removed. The high radiant heat from the crucible melts the solder inside the crystal monitor. Increasing the distance between the crystal monitor and the sample increases the lifetime of the crystal but decreases the accuracy of the thickness measurement. Instead, we estimate the thickness by the time of deposition and confirm the thickness with an AFM scratch test which is outlined later.

Finally, unlike the annealing of SiC to make EG, this sputtering process requires the induction heater to be inside the chamber. This adds complications such as needing a feedthrough, making sure the AC EM fields do not interact with the chamber and the sputtering system is kept cool.

## **2.5 hBN Annealing**

We know from Raman and AFM that well-ordered hBN does not sputter onto the surface. Instead, we need to anneal our sputtered BN to hBN. This requires us to go to high temperatures. Fortunately, SiC can handle these extremely high temperatures and our crucibles that we use to make EG also can withstand these temperatures. The trick is to find the critical temperature with which hBN forms. We measure the crucible temperature from the outside.

As seen in the crystal diagram in fig 15, there is a critical temperature where hBN forms. At atmospheric pressure the critical temperature is 1300°C; however, we find the critical temperature for our BN for a 10-to-60-minute bake is about 1550°C. Higher temperatures also anneal BN, but risk growing more graphene than we want. At lower temperatures than this critical temperature, we find incomplete crystallization of BN. Fortunately, this temperature is also near the temperature where graphene grows. In this project, we tune the time, temperature, and crucible condition to grow EG and anneal BN to hBN.

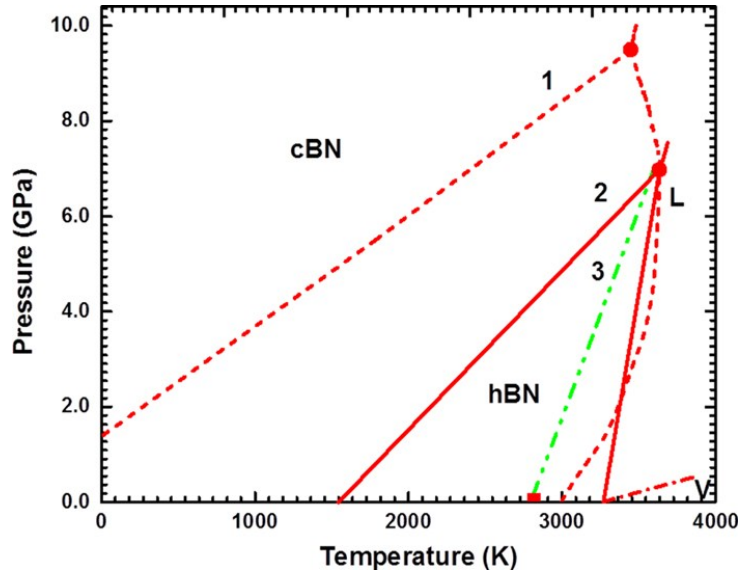
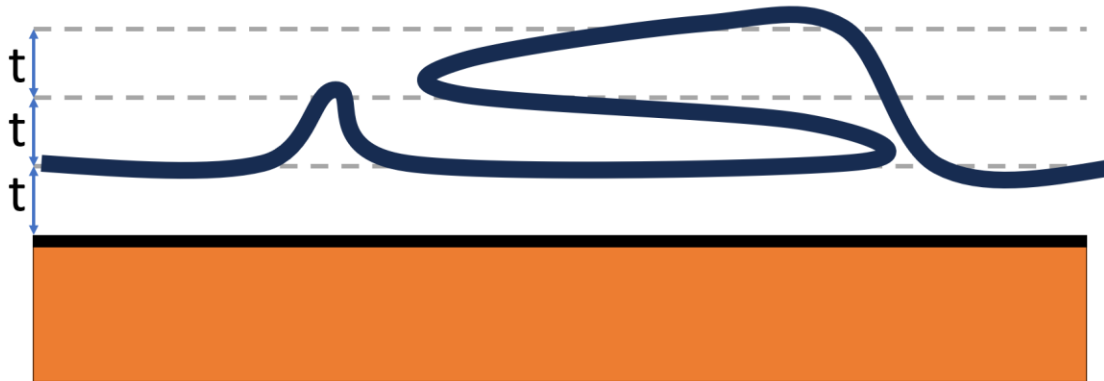


fig 15 Pressure vs Temperature crystal phase diagram for BN. cBN stands for the cubic BN polytype. L is liquid [97]

In fig 15, we see the crystal phase diagram for BN. We work in the 0GPa range in the figure, therefore the critical temperature for hBN is minimized. Incomplete crystallization can be confirmed by Raman, outlined in a later section.

We notice a reduction in the thickness of the BN after annealing of about 20 percent. The exact value is difficult to know due to the uncertainty in measurements between two thickness measurements. We know that a small amount of hBN is sublimated in the annealing process which contributes to a reduction in the thickness of the BN. While

one may expect hBN to sublime at around 3000°C, some literature has shown it can sublime at  $10^{-6}$  mbar [98]. Some of the other contributions are the change in density from sputtered BN, which is made of some aBN, to hBN. aBN density is  $2.28\text{g/cm}^3$ [99] and hBN is  $2.1\text{ g/cm}^3$  which means if mass were conserved, we should see a 8 percent increase in the thickness of hBN compared to our sputtered material. Though, we have not measured the density of our BN films.



*fig 16 Cartoon of different types of pleating and their heights. Larger pleats are three times the height of the thickness,  $t$ , of hBN while smaller pleats are about double the thickness. Orange is SiC. Black is EG, Dark blue is hBN*

The measured thickness is also not considering pleating of the hBN film. If pleating is about 7% of the surface, as measured from a large  $50 \times 50 \mu\text{m}$  scan, and the pleating is a tripling of the material in that region due to three layers of hBN being located at these pleats. Where a diagram of the different types of pleats are shown in fig 16. I estimate that aBN to hBN should result in a 5% reduction in the thickness of the material. The rest of the change in thickness, we suspect, is due to the sublimation of BN, which can be reduced by annealing in an environment already saturated with BN. Such as using a closed crucible that has been saturated with BN and in an argon atmosphere.

## 2.6 Characterization Methods

### 2.6.1 Atomic Force Microscopy

AFM is a method of analysing surface characteristics of a sample. AFM uses a cantilever, with a sharp tip, and approaches the surface of a sample. A laser is directed at the surface of the cantilever reflects then hits a detector. This detector then compares the intensity of the signal across its 4 sections which gives a measurement of the cantilever position.

In contact mode, the tip feels Coulomb-Coulomb interactions between the tip and sample surface which tilts the cantilever up. In this mode, a feedback loop monitors the deflection of the cantilever and adjusts the absolute height of the tip as the surface is scanned to keep a constant deflection of the cantilever and therefore a constant force. The absolute height of the tip, we call the topography measurement, and the adjustment from the feedback loop, we call the error signal. In addition to moving up and down, the cantilever can twist. This twist can be caused by the surface topography or the surface frictional force. Careful subtracting of the left and right scans can remove the topographical data, and we obtain the frictional force. Contact mode has drawbacks. When scanning high frictional force materials such as SiC, wear on the tip is high. To have a scan that completes before the tip is completely destroyed, the scan rate must be decreased, or we can use variable scan rate mode. Variable scan rate mode monitors the error signal and reduces the scan rate when the error signal is high enough. The error signal is used so that when the sample has large topographical variances the tip will slow down at large steps. The drawback of this method is that we lose frictional force data when we do this.

In non-contact mode, the cantilever is driven by a piezoelectric, just off its resonant frequency around 250kHz. As the tip approaches the surface, Van Der Waals interactions cause induced dipoles, which dampen the cantilever's driven oscillation. This dampening changes the resonance frequency of the cantilever and is related to the force on the cantilever which can be related to the tip height from the surface. Then, again, a feedback loop monitors this dampening and adjusts the height accordingly. We can obtain the topography and error signal as in the contact mode, but we also can read the amplitude of the oscillations, and the phase offset from the driven frequency.

The phase offset can be used to differentiate materials. The phase offset is extremely sensitive to the hardness of the material namely Young's modulus. In this way, differing hardness of materials can be differentiated in the NC-AFM and C-AFM.

A new method to this lab to measure thickness is a scratch test. After sputtering BN, the thickness needs to be measured accurately. This can be done with a variety of methods; however, since the exact properties of this recently sputtered BN are not known, the most accurate method is with a scratch test. Ellipsometry has also been tried but does not give accurate results as we do not have the exact physical properties of the sputtered BN to make a good model. For the scratch test, a very sharp razor blade is brought towards the surface, and an "S" pattern is made into the sputtered material. Because SiC is harder than the steel of the razor blade while the sputtered BN is softer than the razor blade, the SiC is left untouched while the pattern is marked in the sputtered BN. Like how a snowplough moves material to the side, the razor blade plows through the BN leaving a large edge of deposited BN. Comparing the height of the lowest point in the scratch (which corresponds to a change in phase in NC-AFM) to the height outside the scratch gives a

good measurement of thickness at that spot on the sample. The “S” shape gives some areas of less deposited material on the inside of the curves of the “S” giving better results than a straight line. The difference in the “S” shape pattern is shown in a diagram in fig 17. Careful consideration needs to be given to the sharpness of the blade, the downward force made during the scratch, and the position of the scan to give good results. The uncertainty of the height is about 0.5nm at worst, which is about the variance in the height of sputtered BN.

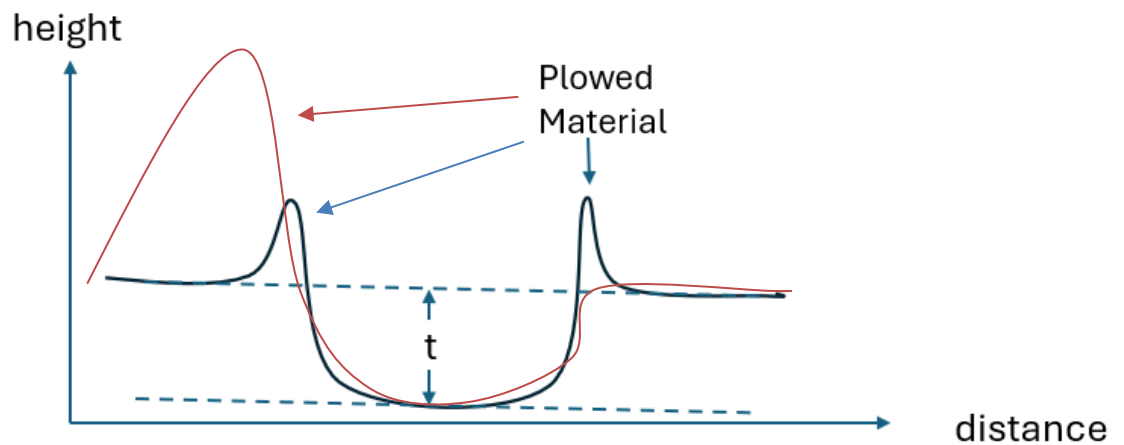


*fig 17 Cartoon of an AFM line scan for a scratch test. The thickness,  $t$ , is measured from the average of the sides of the scan which corresponds to the deposited material and the lowest point which corresponds to the surface of the SiC. Black is representative of a straight slice with a razor blade. Red is representative of regions of an “S” shaped slice.*

### 2.6.2 Raman Spectroscopy

Raman spectroscopy is a well-known non-destructive method we have of verifying the quality of the graphene. Raman involves exposing the surface to a laser and observing the reflected spectrum. As the 532nm laser interacts with the material the electron is excited to the Conduction band. As the photons are absorbed different processes occur inside the material. Phonon and electron transitions can occur inside the material which are determined by the structure and band structure of the material. In this way, a fingerprint

can be made for different materials allowing very quick identification of materials and certain properties. The main transition for EG is called the 2D peak, which commonly occurs at  $2700\text{ cm}^{-1}$ [100]. The other peaks are the G and D peaks. The energy, FWHM, and relative intensities give us valuable information on the quality of the graphene on the surface of SiC [101]. What makes this extra valuable in our case, is that the system uses a standard microscope. Meaning we have control over the focus point. By adjusting the focal point, we can change the relative intensities of SiC, BN and EG to our need.

For graphene the D peak ( $1350\text{cm}^{-1}$ ) corresponds to the boundary between different crystals of graphene and is not a first order Raman effect and only appears in defected graphene [100]The G peak ( $1570\text{cm}^{-1}$ ) corresponds to the in plane vibrational mode.[102] The 2D peak ( $2700\text{cm}^{-1}$ ) corresponds to a different in plane vibrational mode corresponding to two phonons in opposite directions.

For pristine graphene, the picture is simple. A single 2D peak and a G peak[101]. But in bilayer graphene the picture is more complicated because of interactions between the layers. There are now pi and pi\* orbital modes available, that interact to form 4 modes [101]. These modes have different relative intensities and energies, but altogether they make the 2D peak appear broader in bilayer samples compared to monolayer graphene. In this way, we can differentiate monolayer from few layer epigraphene[103].

### 2.6.3 *Cross Sectional TEM*

TEM uses an electron beam to create images of a sample image resolution is on the order of Angstroms and typical energies are around 80keV. Electrons either pass through the sample or are reflected onto a detector. Energy Dispersive X-ray (EDX) spectroscopy

and analysis can also be performed in many systems to obtain the chemical composition of the sample. Cross-sectional TEM involves cutting a slice of the sample and arranging it head on such that a cross section can be measured. Images give information far into the sample and can give information on dislocations, grain boundaries, and stacking faults in 2-D materials. The cutting process is extremely difficult, time consuming, and performed by our collaborators in France, Annick Loiseau at ONERA/LEM .

#### *2.6.4 Low Energy Electron Diffraction*

Low Energy Electron Diffraction (LEED) is performed in UHV. An electron gun is directed at the sample, and we record an image of a phosphor screen of the diffracted electrons. For graphene on SiC, we expect to see diffractions from the SiC and the graphene in a hexagonal pattern. For hBN the crystal structure is almost identical to EG. Similar to previous results, we show that there is no secondary peaks corresponding to hBN for my samples indicating that the BN is either aligned with the graphene or not crystalline[18, 104].

One open question is the orientation of the BN crystal on top of SiC. This may be able to be confirmed with LEED. More testing is needed.

However. Because the EG and hBN should overlap with one another, it is not possible to distinguish between the two definitively[87]. However, if the lattices are mismatched this will be obvious in LEED. There is no characteristic halo of an amorphous material.

#### *2.6.5 X-Ray Diffraction*

X-ray diffraction uses an x-ray source to investigate the crystal structure of materials. In addition, it can quantify strain, dislocation density, and type of material. It can even measure the volume fraction of different crystals polytypes. The process uses Bragg's law, where rays from one layer interfere constructively with a parallel layer. We use x-rays because the wavelength of x-ray's is of the same order as the interatomic distances we seek to measure.

In  $\theta$ - $2\theta$  mode, the sample is held static, and the detector and source are held on opposite ends of the sample. The detector and source are the same, but opposite angle above the plane of the sample. The resulting data is a shown in angle vs counts. Peaks in the data correspond to the angle from Bragg's law. Models can match unknown materials to the data, assuming the model is in the database.

Thin films are exceedingly difficult for XRD to measure. There is simply so little material for the detector to measure, and the substrate dominates the signal. There are solutions. Increasing the area measured, increasing the thickness, and increasing time are all ways to increase the count rate of the detector. A small scan can take an hour, though can easily go for 8 hours for a sample of typical thickness(5nm).

#### *2.6.6 X-Ray Photoelectron Spectroscopy*

X-rays can also be used to identify the chemical makeup of a material. The process uses the photo-electric effect. X-rays irradiate the sample and cause electrons to be ejected from the sample. These electrons have an energy related to the elements and the bonding energies inside the sample. While there is a penetration depth of the x-rays of 20 to 100  $\mu\text{ms}$ , we are limited by the photo-emitted electrons going through inelastic collisions inside

the sample and not reaching the detector. For this reason, XPS is sensitive to the surface of the material, typically the first 5-10nm. The emitted electrons must be collected, so UHV is typically used for XPS.

XPS can be a destructive measurement because of the heat and electrons emitted changing the molecular bonding inside the material but is non-destructive in general. However, XPS is sometimes used with ion etching, which can give a chemical composition as a function of height.

## **2.7 Fabrication Methods**

### *2.7.1 Electron Beam Evaporation*

E beam evaporation involves heating a metal with an electron gun till it evaporates metal onto the sample. In a typical setup, electrons are emitted by a filament and redirected to the target using permanent magnets. Electromagnets provide fine adjustment of the beam onto the target. Furthermore, the electromagnets sweep the field in a pattern such that the electron beam moves smoothly over the target surface to enable even heating of the target. There are a variety of complications that must be accounted for. This process must be done in high vacuum minimum  $1 \times 10^{-6}$  mbar to increase the purity of the materials, to increase the lifespan of the filament. Ideally, we want the pressure of the chamber to be much less than the vapor pressure of the target during heating. Furthermore, the sample should be sufficiently far away from the target such that material from the target such that rays from the target to the sample are parallel. There is always a crystal monitor and a shutter to enable precise and accurate film thickness, on the order of 0.1 nm. In our setup, we have multiple crucibles with different metals, typically, Pd, Au, and Al. Al should

always be kept in vacuum otherwise a thick  $\text{Al}_2\text{O}_3$  layer forms that has a much higher melting point than Al, and evaporating Al would prove difficult if not impossible without enough heating power.

In addition, while evaporating Al we can begin to evaporate, with the shutter closed and introduce oxygen to a pressure of  $5 \cdot 10^{-5}$  mbar. As the Al atoms travel towards the sample the mean free path of the atoms is such that once the Al atoms reach the sample, we are depositing  $\text{Al}_2\text{O}_3$ .

When depositing very thin layers  $< 50\text{nm}$  the wetting of the materials needs to be considered. At small amounts of deposition, nanoparticles of the deposited material form, instead of a thin layer. For very thin layers other methods such as ALD might be able to be used.

In addition, depending on if the previous step introduced an undercut. The sample should rotate at an angle to get material in all the undercuts.

Then there is the issue of Aluminum. Aluminum forms an oxide layer on the surface upon being exposed to the atmosphere. When this happens, the Alumina layer blocks the incoming electron beam from heating the Aluminum. There are many ways to avoid this, but our homebuilt system suffers from this condition leading to previous results having a lower-than-expected dielectric constant for the alumina layer. Due to a design error in the water-cooling system, crucibles could not remain in the chamber between depositions with different materials. This resulted in the aluminum becoming oxidized more than desired and leading to low quality dielectrics. Fortunately, this has been fixed.

### 2.7.2 *Reactive Ion Etching*

RIE Reactive Ion etching is a form of dry etching used commonly in the semiconductor industry. The sample is placed on an electrically isolated holder, such as Alumina. Low pressure reactive ions are introduced into the vacuum system and a plasma is generated using an RF source. The plasma used changes depending on the material to etch. Our lab uses O<sub>2</sub> or SF<sub>6</sub> depending on the material. As electrons move inside the chamber some are lost to the sides of the grounded chamber, and some are donated to the sample surface. The more massive positively charged ions then migrate towards the sample surface from the Coulomb effect and react with the sample surface where they are then pumped away by a rotary pump. The ions have enough kinetic energy to overcome the potential energy of the surface bonds. The energy of the plasma ranges from as little as 10 Watts to hundreds of Watts of power. By controlling the time, energy, pressure, and gas flow rate, researchers can control the rate of etching to just less than the nanometer size scale.

In addition, we can increase the directionality of the etch by adding an external electric field to accelerate ions to the sample surface. In this regime, we do not rely on donating electrons to the sample to migrate ions to the sample surface. This process is known as ICP and can be done in the Marcus cleanroom. This type of etch is more directional than RIE and etching happens in a normal direction to the sample surface.

We can use RIE to build novel devices using oxygen and Sulfur hexafluoride plasma. The three materials in our devices, BN, graphene, SiC, have differing properties for etching. BN and SiC are etched by SF<sub>6</sub>; however, graphene is not etched by SF<sub>6</sub>, but

rather fluorinated. In this way, graphene terminates the etching process when we have a BN/EG/SiC stack, exposing the graphene and giving us an electrical contact to adhere to.

A table of measured etch rates is shown in fig 17.

Material	(4.0cc/min) SF6 100W	(4.0cc/min) O2 16W	(3.2 cc/min) SF6+(0.8 cc/min) O2 100W
SiC 4H Si face	~0.1nm/sec	0*	1.4nm/sec
BN sputtered	1.4nm/sec	0	1.4nm/sec
hBN	1.4nm/sec	0	unmeasured
Epigraphene	0**	Etched in <2sec	Etched in <2sec

*fig 18 Table showing different measured etch rates in our RIE machine. \*an oxygen etch on the surface of SiC Si face results in a difficult to remove SiO layer which may roughen the surface. \*\*Epigraphene which is exposed to SF6 becomes fluorinated which can be removed by annealing.*

### 2.7.3 Atomic Layer Deposition

ALD is a method to grow thin films with a uniform coating onto a sample. In ALD, a gas precursor is introduced to the surface where a monolayer of the precursor is formed. Then, the gas is purged, and the next precursor is introduced which bonds to the previous layer. The growth is self-limiting giving conformality and uniform thickness across the sample. It is used in a variety of industries including the microelectronics industry, photovoltaics, as well as biotechnology. The uniformity of the coating makes it an ideal case for gate dielectrics.

There is one difficulty when combining ALD with 2-D materials. Since many 2-D materials such as hBN and graphene do not have available bonds for the initial precursor to latch onto, deposition is either impossible or centered at defects in the surface. Other solutions have been found to allow for ALD to be used on 2-D materials such as a seed layer using e-beam deposition or an intermediary dielectric such as PTCDA.

### 2.7.4 PTCDA Deposition

2-D materials like graphene and hBN are difficult to perform ALD on to achieve a high-quality dielectric for a gate. One method of combating this issue is to coat the 2-D material with a thin interstitial layer, such as PTCDA. PTCDA is an organic Semiconductor with a bandgap of 3.3eV depending on the depositing conditions.[105, 106] While not a high  $\kappa$  dielectric by itself, PTCDA adheres extremely well to graphene thanks to its similar hexagonal structure. PTCDA has been used previously as an anchoring layer and has shown reliable results on graphene. [105-107]When deposited correctly, PTCDA forms layers on top of the graphene. The time of deposition, the temperature, and the temperature gradient can be tuned to achieve a consistent number of layers on the surface. The process can be controlled to deposit 1-8 monolayers of PTCDA. Fortunately, PTCDA gives a strong Raman signal. Raman done on PTCDA shows a strong fluorescence, indicative that the PTCDA is not ordered when deposited on SiC as shown in fig 19.

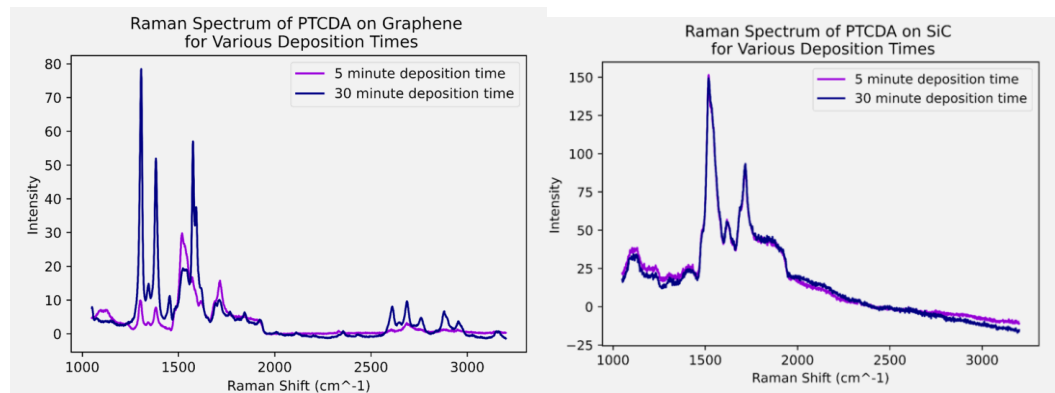


*fig 19 PTCDA Raman signal on Epigraphene and SiC. Fluorescence is indicative of a nanocrystalline or amorphous material, while the sharp Raman peaks on Epigraphene indicates crystallization on the EG. Credit: Marygrace Fagan*

After coating with PTCDA, ALD creates a homogenous layer, with complete coverage over the surface of the sample.

Since PTCDA is intended to directly contact graphene, earlier work in this lab has shown that PTCDA reduces the charge carrier density. PTCDA on hBN on graphene needs to be researched. Preliminary results are presented in 3.2.

## 2.8 Low Temperature Transport

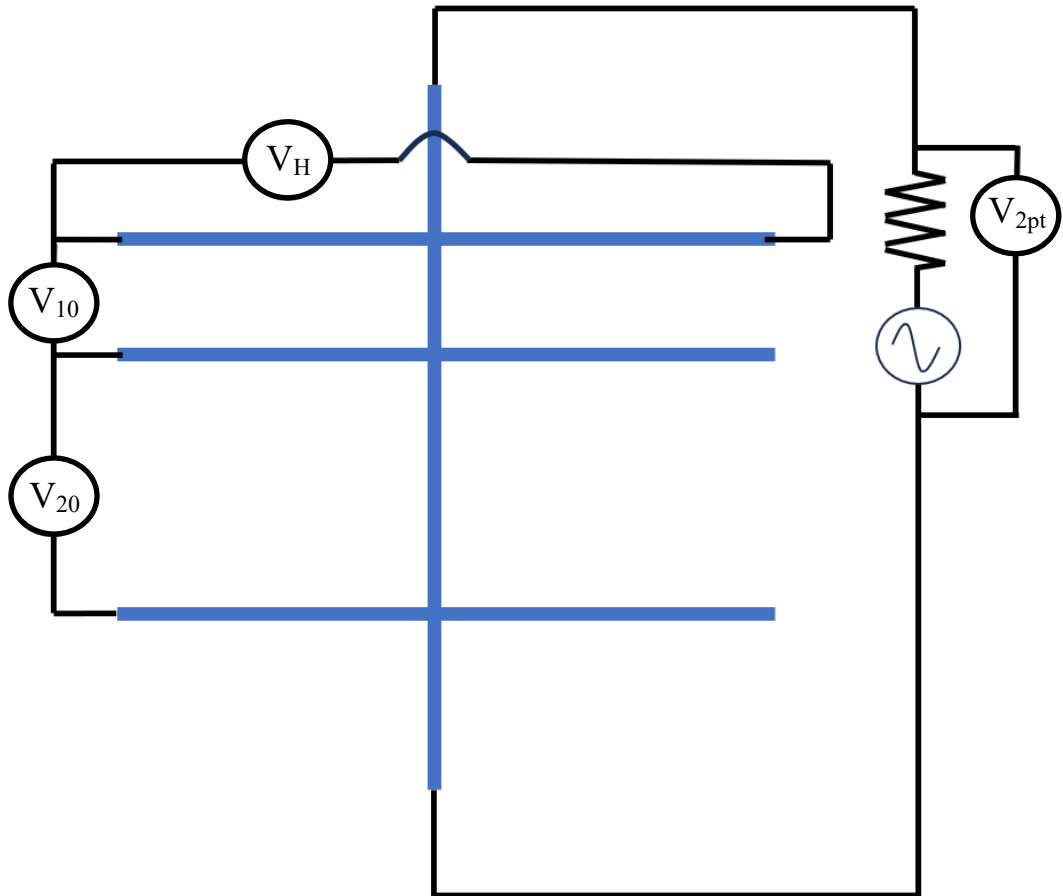


*fig 20 Schematic of Hall bar measurement  $V_{2pt}$  for Voltage across sample,  $V_H$  for Hall Voltage, and  $V_{10}$  and  $V_{20}$  for voltage across the  $10\ \mu\text{m}$  and  $20\ \mu\text{m}$  lengths. The series resistor,  $R$ , is chosen to be much greater than the resistance of the Hall bar such that we have a measurement of the current through the Hall bar.*

Electron transport measurements are done using Stanford Research lock-ins with a large resistor ( $10\text{M}\Omega$  typically) in series with the sample. The lock-ins have a  $10\text{M}\Omega$  to

ground resistor at the inputs. The lock-ins are connected via BNC connector to switchbox equipped with noise reduction and then connected to cryogenic wires to the sample mount.

A diagram of the Hall bar is shown in fig 20. The devices are made to measure some key properties of the material. A Hall bar is made to measure square resistance, mobility, and charge carrier density. When the resistance of the series resistor is much greater than the sample, we can say:

$$I_{IN} \approx V_{IN}/R_{IN} \quad (10)$$

$$R_{\square} = \frac{V_L}{I_{IN}} * \frac{w}{L} \quad (11)$$

Where L refers to the 10 or 20  $\mu\text{m}$  lengths and w is the width across the Hall bar.  $R_{\square}$  should be constant for a diffusive conductor. If  $R_{\square}$  is not constant something else is going on such as the existence of ballistic transport from the edge state, assuming the graphene is homogenous across the sample.

$$n = \frac{V_H}{I_{IN}e} = \frac{R_H}{e} \quad (12)$$

$$\mu = \frac{V_H}{I_{IN}B} * R_{\square} \quad (13)$$

Where  $n$  and  $\mu$  are the charge carrier density and mobility, respectively. Here we consider ungated graphene. To get to these low temperatures we use a He<sup>4</sup> Cryostat. The concept is like how a typical refrigerator works. By compressing the He to high pressures, typically 250PSI, we can pump the He into a small chamber which is then rapidly allowed

to expand which decreases the Helium temperature which then absorbs the heat from the environment. This process repeats over and over making a characteristic expanding gas sound and a bang from the piston. This cryostat is a 2-stage cryostat which will take the gas to its lowest temperature of just less than 4.2K. But we can go lower.

We can achieve lower temperatures via evaporative cooling. By injecting cold He gas through a needle valve and pumping of the outer space we can get to temperatures around 1.5K near the boiling point of He.

To go to these temperatures is quite easy. The next sections will go into more detail.

### 2.8.1 Dip Stick

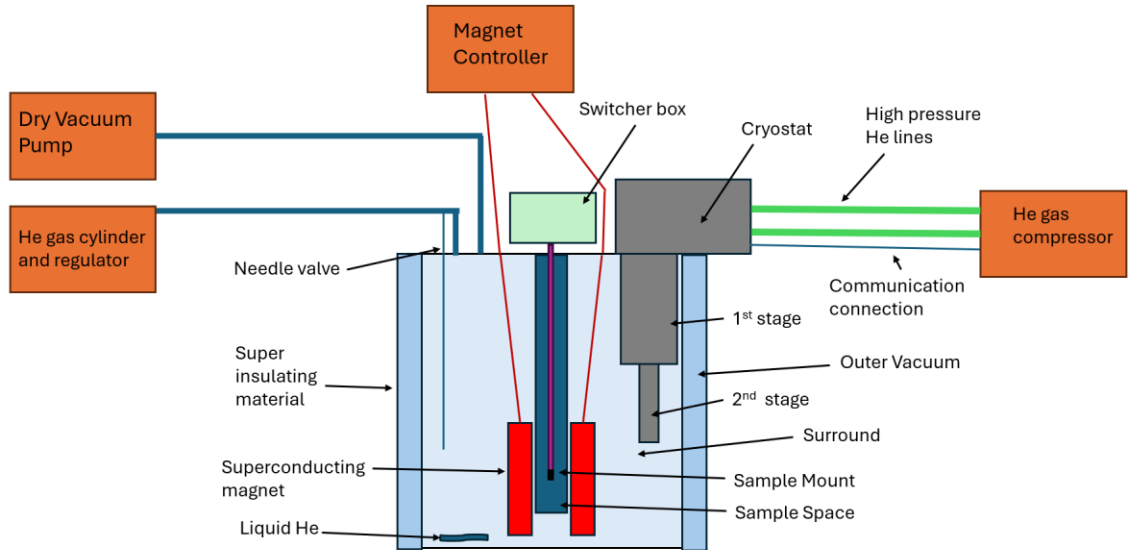


*fig 21 Block Diagram of cryostat, Not pictured: thermal connection between 2nd stage and magnet, pumping system for outer vacuum, temperature sensors, sample heater and heater control.*

A cartoon of the cryostat is shown in fig 21. The sample must be mounted securely to stay in place while we ramp the magnet to 9T and handle thermal shocks. To that end phosphor bronze cables connect the sample to the switcher box above. These wires are coated in an insulator specifically designed to withstand the vibrations and thermal stress a cryostat can create. Despite this, they still fail. So, we must always test the wires before and after a run to make sure they are still working.

Next the sample is wrapped in a super insulator foil. The inside is a thermal and electrical insulator while the outside is conductive to reflect radiation from the environment away from the sample. In addition, the dip stick must be passed through a series of baffles which further restrict blackbody radiation and convection from reaching the cryogenically cold areas. The dipstick also is equipped with a thermometer and a heater which together can control the temperature of the sample via a PID controller. In addition, every time we cool down, we build a small Kapton tape cage which prevents the superinsulation from touching the wires of the sample.

The switcher box is just as it sounds. It takes the wire through a filter to a switch. In this way we can isolate individual samples while we are testing, and we can have samples grounded when we are not testing them.

### *2.8.2 Cryostat*

The cryostat consists of a body and the head. The body is outside the chamber and is at room temperature. It houses a 2-phase motor which is controlled by the He gas compressor. Having rebuilt a cryostat myself, most of the heft of the cryostat comes from the windings

of this motor. The motor is held separately and couples with the piston assembly which moves us to the head.

The head has a lightweight piston which is connected to a rotational to linear mechanical converter. The incoming gas goes up inside of the piston and goes to the first stage chamber. On the next cycle, that same gas will flow up the 2<sup>nd</sup> stage piston, which is mechanically connected to the first, where we reach its ultimate cooling capacity before being pumped away or rather pushed out due to the difference in pressures. This whole assembly is then covered with a stainless-steel body and secured using a high-pressure seal.

The cryostat has two common metrics. Cooling power at 300K and cooling power at 4.2K. The cooling power at 4.2 K determines how much we need to protect the cryogenic area from the environment.

### 2.8.3 Lock-ins and Measurement

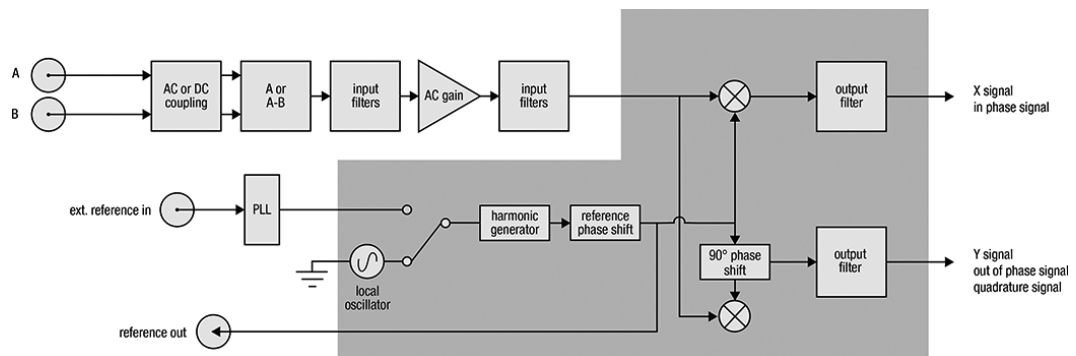
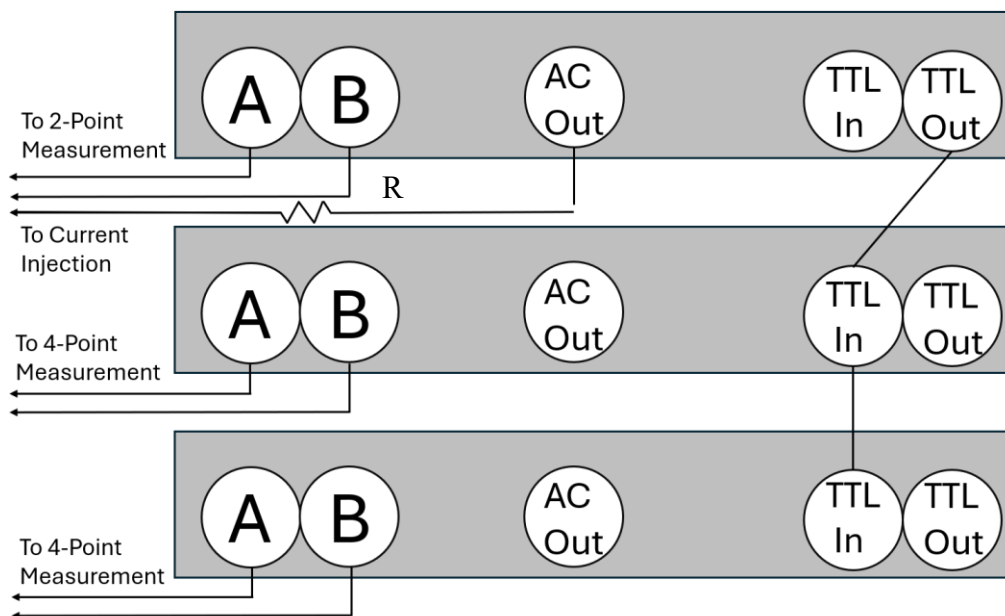


fig 22 Block Diagram from Lake Shore Cryogenics showing a typical lock in amplifier. [108]

While some systems can benefit from DC measurements, we typically use Lockins which measure an AC signal against a reference AC signal. Where a lock in is designed like fig 22 and a setup with BNCs is shown in fig 23.



*fig 23 Typical setup for measuring a Hall bar. The series resistor,  $R$ , chosen to be much greater than the sample resistance.*

## CHAPTER 3. BN/EG/SiC DEVICE FABRICATION

### 3.1 Heterostructure Preparation

#### 3.1.1 BN Anchoring

NC-AFM is the preferred method to look at hBN heterostructures as there may be exposed SiC which would damage a C-AFM tip, NC-AFM reveals that sputtered BN is inhomogeneous as expected from a sputtered material. After annealing the BN becomes atomically flat except for pleats in the surface, which is indicative of recrystallization of BN into a 2-D material namely hBN. Line scans of the pleats reveal that the height of the pleats are about two times or three times the thickness of the hBN. hBN has a negative thermal expansion coefficient in the in-plane direction and SiC has a positive thermal expansion coefficient. When hBN is annealed at high temperature and begins to cool, the SiC shrinks, while the hBN expands outwards. If the BN is pinned at certain places on the SiC, pleating is inevitable.

This brings us to an interesting consequence of the pinning of BN. When there is no pattern on the BN when annealing, the BN becomes extremely likely to flake off during transport. There were several times when preparing an hBN sample for XPS or XRD the hBN would be able to be seen in AFM and Raman; however, in the process of transporting from the Howey physics building to the Marcus nanotechnology building, the hBN would disappear. Similar samples shipped to France would lose their hBN layer during transport. For transporting it is necessary to make sure the hBN is adhered to the SiC via etching. A

grid pattern can be etched into the BN/SiC samples before annealing to make sure the hBN is well adhered to the SiC so transport can happen. The exact mechanism is not known.

Pleating is a consequence of the pinning effect at high temperature. As the hBN cools it expands along its plane resulting in pleats that are determined by where the edges of the BN are. In fig 25, the pleats are clearly determined by the shape as the pleats are perpendicular to the edges of the Hall bar, while in fig 24, the pleats are allowed more freedom as there is less restriction from the edges.

That being said, hBN has no out of plane dangling bonds and the B-N bonds do not cause polarization between either side of the sheet. At the edge of hBN there are bonds available to bond to SiC perhaps forming Si-N bonds.

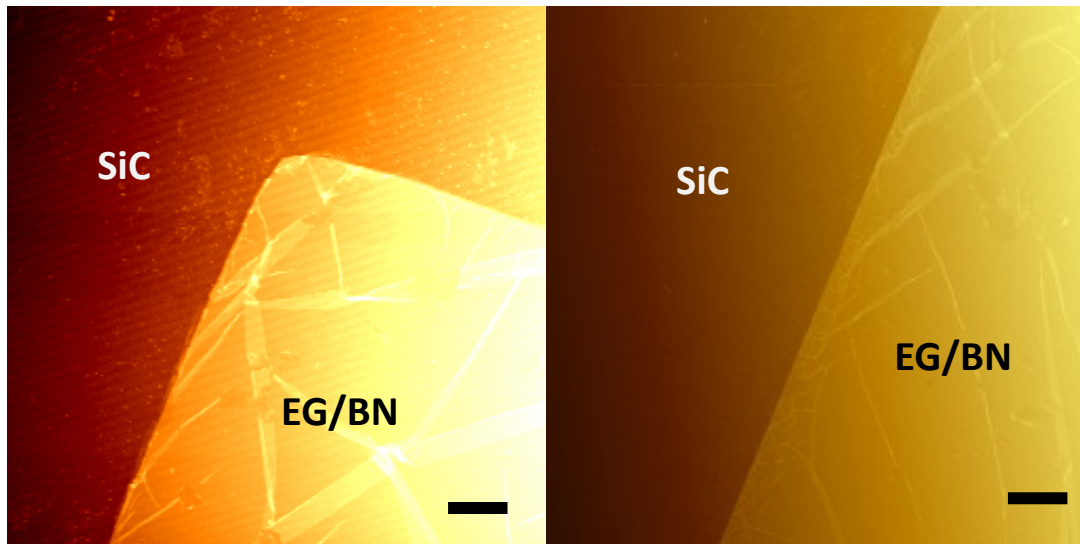


*fig 24 NC-AFM scan showing 6nm thick hBN square with pleating at edges. 90X90 μm scans with 10 μm scale bar*

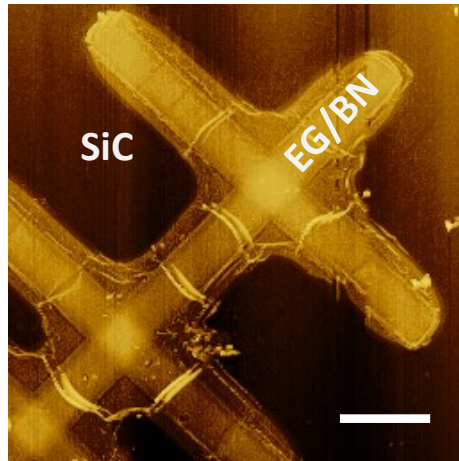


*fig 25 NC-AFM scan showing 10  $\mu\text{m}$  and 20  $\mu\text{m}$  leg Hall bar hBN with pleating at edges. 8  $\mu\text{m}$  scale bar.*

### 3.1.2 SiO

One issue we face is getting sputtered BN to stick to SiC. As SiC is exposed to the atmosphere, SiO forms on the surface in a matter of minutes. During annealing, the BN will disappear from the surface of the SiC, leaving only EG/SiC. This mechanism is attributed to the SiO on the surface of the SiC on the Si face. The exact mechanism is unknown, but we suspect the oxygenated surface prevents bonding with the substrate. There are a couple of ways to combat this. The first is to have a high temperature vacuum annealing to remove the SiC. Annealing for 30 minutes at 1250°C and then immediately depositing BN in situ normally causes the BN to stick. While a longer time should give more reliable results of the BN adhering, due to size of our chamber 30 minutes at 1250°C is the longest we can feasibly bake for.

The second solution is to gently roughen the surface of the SiC, via SF<sub>6</sub> RIE. And then remove any remaining oxygen with a high temperature anneal. While this method does adhere the BN to SiC, the roughening of the surface would cause disordered graphene to grow when annealed.

## 3.2 Heterostructure Characterization

### 3.2.1 BN Raman

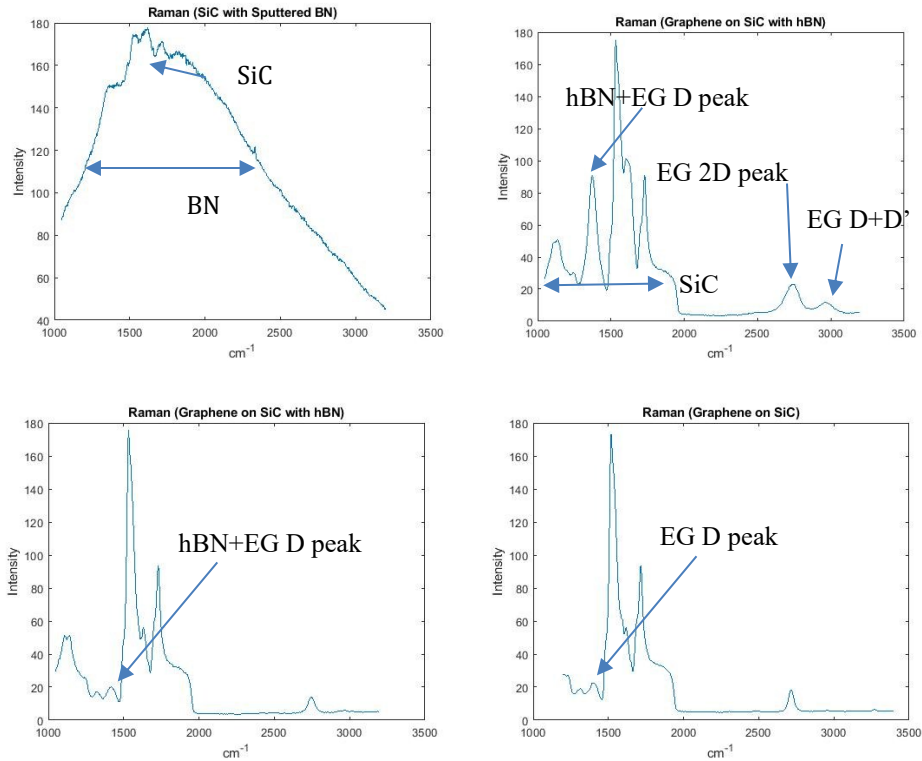


fig 26 Typical Raman for various samples. A) 6nm Sputtered BN B) 50nm annealed hBN with EG C) 4nm annealed hBN with EG showing a small amount of broadening of the 1350 peak D) monolayer EG thanks to Yue Hu

Representation Raman spectra are shown in fig 26. For hBN the only observable peak is at  $1366\text{cm}^{-1}$ [109] and corresponds to the in plane vibrational mode analogous to the graphene G peak. The cBN peak at  $\sim 1050\text{cm}^{-1}$  overlaps with strong SiC peaks and is impossible to see on our samples. Other Raman signatures we see is BN fluorescence after sputtering whose FWHM  $>1500\text{cm}^{-1}$ . This signal goes away after an annealing indicating crystallization of the BN.

One fundamental problem in identifying hBN is the small Raman signature at our thicknesses. There is almost no response from hBN[109], and the main peak of hBN overlaps with the D peak of graphene. This overlap is being investigated, and we are investigating a method to differentiate the contribution from h-BN vs. graphene in the Raman data.

### 3.2.2 XRD and XPS

A sample of BN was sputtered on SiC and annealed in such a way where we anneal the hBN, but do not grow graphene. We then compare this XRD data against bare SiC and unannealed BN to observe the hBN peaks. hBN has a characteristic peak at  $26.4^\circ$  (002) as shown in fig 27 and a smaller one at around  $40^\circ$  (100) which is unobservable in our samples. The Lorentzian fit is centered at  $26.44^\circ$  which verifies our BN has been annealed to hBN when compared with literature.

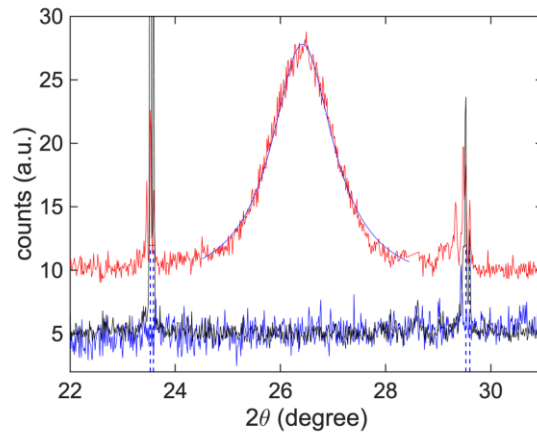


fig 27 X-ray  $\theta$ - $2\theta$  spectra for hBN (Cu  $K\alpha_1$  -  $K\alpha_2$  source) for red. A Lorentzian fit is shown as a blue line. Unannealed BN in black and bare SiC in blue. The vertical lines are the 6H-SiC peaks (0001) (multiplicity  $m=4, 5$ ).

In XPS, we see boron and nitrogen peaks which we compare to a commercially available sample in fig 28. Our smaller FWHMs are due to our samples being much thinner than the others and as such we have fewer attenuated electrons from deeper in the sample

resulting in less scattering from the x-rays that penetrate deeper into the material [110]. In addition, we see a small peak which corresponds to  $\pi$ - $\pi^*$  as seen in hBN.

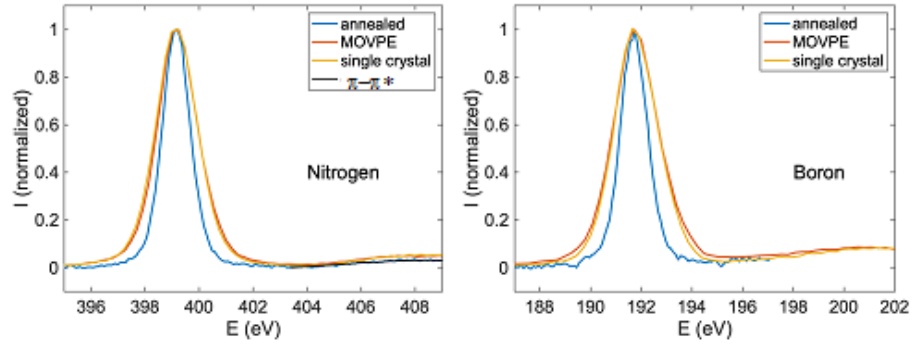


fig 28 XPS spectra for hBN thin film. Which agrees with single crystal hBN commercially available. The  $\pi$ - $\pi^*$  satellite peaks confirm  $sp^2$  bonding. The annealed peaks were shifted by about 1eV to match the h-BN single layer crystal peaks; the shift could be due to the different experimental conditions between measurement systems or it could be that our sample is better able to conduct electrons away from the sample quicker due to a buffer layer at the interface of the SiC and hBN leading to less charging of the surface.

### 3.2.3 BN Cross-Sectional TEM

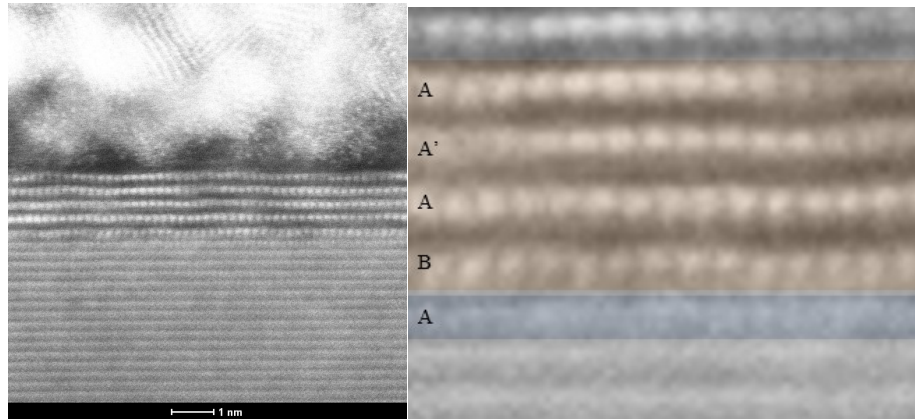
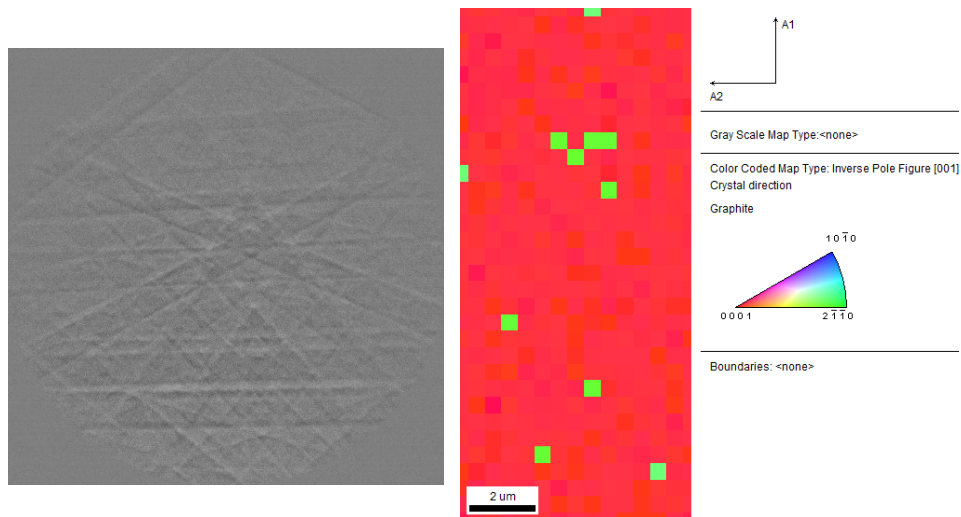


fig 29 Preliminary results showing hBN on buffer layer on SiC. The right image is a zoomed in guess of the stacking structure from a region in the left picture.

The images in fig 29 were performed on samples with no graphene, but there is most likely a graphene buffer layer. hBN normally exhibits AA' stacking while graphite is AB Bernal stacking. If we consider the Buffer hBN stack, we see ABAA'A on most of this cross-sectional area, which is expected. More samples and thicknesses need to be done. Thicker layers should be made to better see the stacking order Furthermore, we are still waiting for the EDX results of this image, so more data will hopefully be made available soon.

### 3.2.4 EBSD

To circumvent this charging issue from LEED, we can use electron backscatter diffraction (EBSD) to measure the lattice constant and lattice orientation of annealed BN samples.



*fig 30 EBSD results (performed by Yang Su). To the left is a sample Kikuchi pattern and to the right is a fit to a model. The green regions are errors in the model. We notice that all the hBN is in the 0001 direction.*

The above sample had BN sputtered then annealed in a highly confined environment such that no graphene grew, while the BN was annealed. LEED was impossible as the BN was insulating. We see in fig 30 that the BN is lattice matched with the underlying SiC, and thus would be matched with graphene, if graphene had grown on this sample.

### **3.3 Device Fabrication**

#### *3.3.1 Charging Issue*

During e-beam lithography electrons bombard the surface and accumulate in the material. If the material is a conductor, the electrons will be swiftly moved away from the target area, eventually being redirected to the ground plane in the system. In our first lithography step where there is unannealed BN on top of SiC, the electrons will accumulate redirecting the beam which will cause erratic drifts in the pattern.

This charging issue is a well-known problem for e-beam lithography. There are a variety of solutions that have been found. The use of a conductive layer above or below the resist can be used. A product called ESpacer which is a conductive polymer solves the problem. Another method is Variable Pressure EBL where a gas such as N<sub>2</sub> is introduced to the system and the use of differential pumping is utilized to maintain low pressure in the beam column. While the exact mechanism is not known, there are two effects for lithography that this can have; the positive gas ions created by the beam balance out the negative charges at the surface; the gas scatters the electrons creating a beam skirt which spreads the charge across the surface.

While these methods work, they were not available to me at the time. A different solution had to be found. The main factor to controlling the charging is amount of charge deposited at a point in a given time. By changing the beam current to low values, 5-10pA, we could eliminate the charging effect from the surface. This method is available to our shared system on the fourth floor of the Howey Physics building but is not available to us for the cleanroom e-beam system. For these relatively large structures, the time to make a pattern is long, as we would typically use 6nA for this size of structure.

### 3.3.2 EG Contacts

A fundamental problem with EG under hBN is making electrical contact with the graphene. In this section, I will present the 5 methods we have found to contact the EG and the pros and cons of each. These are listed in fig 31. There is a common issue with all but one of these contacts. They are capacitive junctions, except for EG to FLG connection.

Method	300K Contact Resistance Estimated	4K Contact Resistance Estimated
1. O <sub>2</sub> RIE w/hBN mask +Pd/Au	Inconsistent	Not Tested
2. SF <sub>6</sub> +O <sub>2</sub> RIE w/MaN mask +Pd/Au	10kΩ	Insulating
3. BCl <sub>3</sub> +Cl ICP w/Alumina mask +Pd/Au	10kΩ	Insulating
4. SF <sub>6</sub> +Pd/Au	1kΩ	10kΩ
5. EG to FLG	70kΩ	70kΩ

fig 31 Table of different methods for electrical contacts

### 3.3.3 O<sub>2</sub> RIE w/hBN mask +Pd/Au

Method 1 was the first and simplest method detailed infig 32. After annealing the Hall bar structure, the hBN is used as a mask for RIE etching with oxygen. Then, a

Pd/Au layer is deposited with e-beam evaporation such that the metal overlaps the hBN, hopefully contacting the EG.

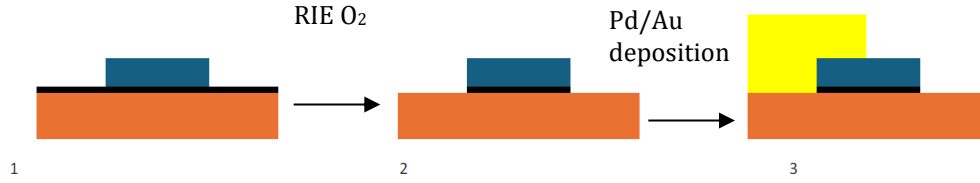


fig 32 Process flow for the  $O_2$  RIE w/hBN mask +Pd/Au. Orange: SiC, Black: EG or FLG, Blue: hBN, Yellow: Pd/Au

I attempted to make Van der Pauw measurements with this method; however, large contact resistance coupled with low mobility  $<10 \text{ cm}^2/(\text{V}\cdot\text{s})$  made measurements unreliable. Contact resistance ranged from  $20\text{k}\Omega$  to  $100\text{s of M}\Omega$ . This inconsistency was attributed to over etching of the EG. To optimize the etch time, lower etch times were used; however, we saw trivial improvement.

### 3.3.4 $SF_6+O_2$ RIE w/MaN mask +Pd/Au

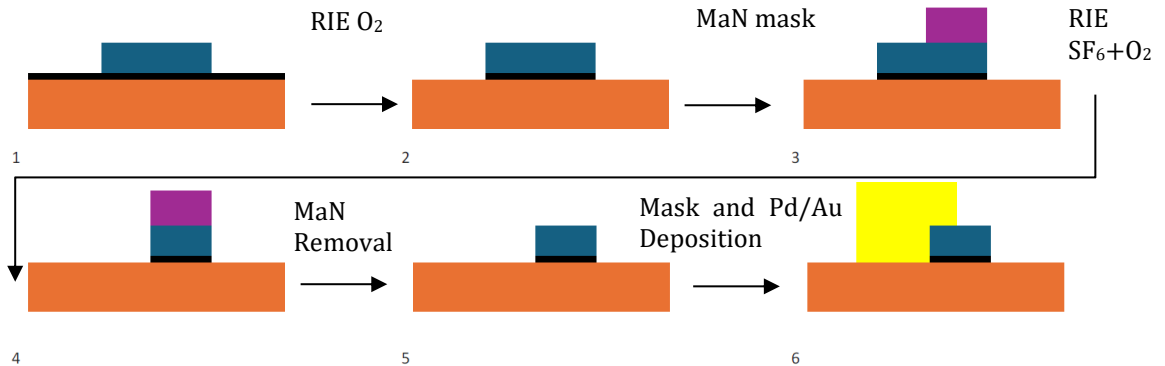


fig 33 Process flow for " $SF_6+O_2$  RIE w/MaN mask +Pd/Au" and "ICP etch and Pd/Au" Orange: SiC, Black: EG or FLG, Blue: hBN, Yellow: Pd/Au Purple: Mask

Side contacts can be done by a variety of methods. Method 2, I outline here and in fig 33 is a simplified method. After the hBN shape is etched and annealed we have

graphene under the hBN and FLG (stacking order has not been confirmed yet) outside the hBN shape. Next, we oxygen etch the entirety of the sample using the hBN structure as a mask for the graphene underneath. Using e beam lithography and RIE etching we cut into the hBN using MaN as a mask, hopefully exposing a graphene edge. Then, we deposit Pd/Au in a 150nm/150nm stack such that the metal contacts will slightly overlap the hBN shape. These shapes show  $\sim 10\text{k}\Omega$  contact resistance at room temperature. However, when these same samples were put into the cryostat, the contact resistance increased to over 10 giga-ohms, which we are not equipped to measure. This final contact resistance was measured with a voltage divider, a 9V Alkaline battery, and a picoammeter, whereas the temperature-dependent measurement was made with a  $10\text{M}\Omega$  to ground lock-in amplifier with all the error at high resistances that entails.

This behaviour is indicative of a capacitively coupled contact. One explanation is that when we go to low temperature, the material shifts via thermal expansion. hBN is expanding over the surface of graphene filling in more of the gap between gold and graphene. TEM results would give more validity to this hypothesis. The change in resistance is not due to the change in temperature changing the dielectric constant of hBN as hBN has a stable dielectric constant as a function of temperature [111].

### 3.3.5 ICP etch and Pd/Au

Method 3 is another way to make side contacts that was perfected by Yue Hu. By using ICP with  $\text{BCl}_3$  instead of RIE a 90-degree cut can be made into the hBN/EG/SiC stack. Using Alumina as a mask, ICP exposes the EG so that a Pd/Au contact will come

into contact on the side of the EG 1-D contact. This method has been successful with EG on SiC.

For hBN/EG/SiC the process is identical to the EG/SiC method except instead of  $\text{BCl}_3$ , we use  $\text{BCl}_3+\text{Cl}$  to better cut into hBN. The resulting contacts are acceptable at room temperature but quickly become insulating as the temperature decreases to 4K mimicking the behaviour of the RIE etch side contacts.

### 3.3.6 *Why Do Side Contacts Work in Other Systems?*

Many other systems have used side contacts to remarkable success. hBN/EG/hBN heterostructures have remained conducting at low temperature. In addition, our lab has used  $\text{Al}_2\text{O}_3/\text{EG}/\text{SiC}$  side contacts to remarkable success. The difference in our example is the pinning of the graphene. The EG is pinned to the SiC. As the system cools after annealing, the EG moves with the SiC, while the upper layers of hBN expand increasing the space between the contact and the EG. In other words, it is the combination of SiC and hBN and their differing thermal expansion coefficients which make side contacts impossible. It is not clear where the bonding happens between the SiC, Au/Pd, hBN, and EG, but the exponential increasing of resistance with decreasing temperature is indicative of a capacitively coupled contact. In addition, as the frequency was increased on the lock-in amplifiers the side contact's resistance increased as well.

### 3.3.7 SF<sub>6</sub> RIE

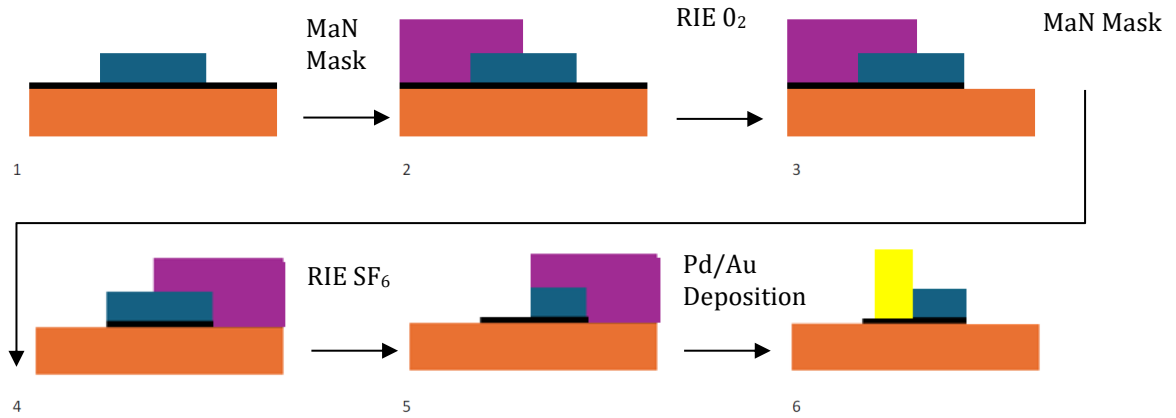


*fig 34 Process Flow for SF<sub>6</sub> RIE Orange: SiC, Black: EG or FLG, Blue: hBN, Yellow: Pd/Au Purple: Mask*

Fluorine gas has proven to be effective at etching BN and is an effective method of exposing the EG to the environment. Method 4, detailed in fig 35, exploits this. Upon being exposed to fluorine EG becomes fluorinated graphene, which is a semiconductor. Fluorinated EG may be annealed to become unfluorinated EG, but that was not evaluated in our system.

The idea becomes to etch hBN to expose the EG and use the EG as a etch stop, where the etching self terminates as all the hBN is etched away. Unfortunately, SiC is also etched by SF<sub>6</sub> very slowly, enough such that the timing of the etch must be carefully timed and tuned such that the SiC underneath the EG is not etched away and the exposed fluorinated EG flakes off.

### 3.3.8 EG to FLG

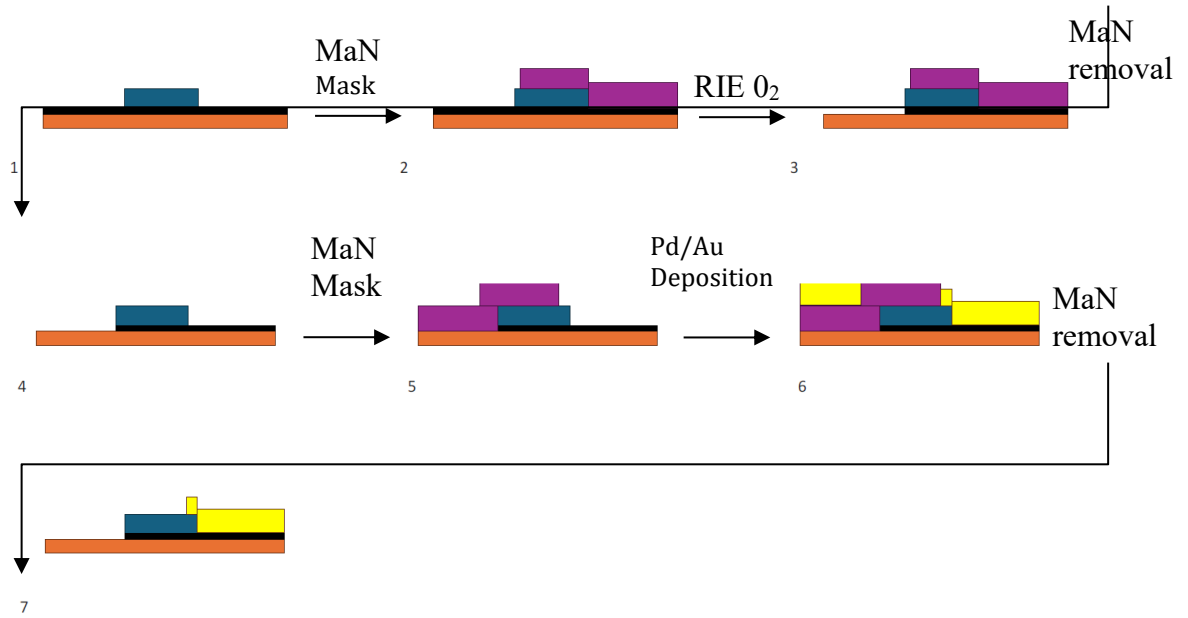


*fig 35 Process flow for EG to FLG contacts. Orange: SiC, Black: EG or FLG, Blue: hBN, Yellow: Pd/Au Purple: Mask*

Method 5, shown in fig 35, which is actually the second method tried and the most successful way to contact EG under hBN was to use FLG to bridge the gap between EG and the metals. During the annealing process, FLG forms outside the BN structure. This is because that area has been roughened via SF<sub>6</sub> RIE etching. The greater surface area allows more Si to escape the surface and leads to more graphene formation. Whether this carbon outside the BN is FLG or graphite was not determined.

## CHAPTER 4. TOWARDS LARGE MEAN FREE PATH

In this chapter, I will discuss how we made sample X1CBA2, then I'll show the raw data from low temperature transport measurements. Finally, I'll discuss how we do the analysis of this sample and the results of this analysis.

### 4.1 Hall Bar

This sample was cleaned with acetone and IPA sonication and RIE O<sub>2</sub> 16W for 60s to remove any residue left over. Next, the sample was brought to 1250°C for 20min and then reduced to 400°C. The Hall bar was etched with RIE SF<sub>6</sub>+O<sub>2</sub> 100W such that the ZZ was along edge of the body of the Hall bar. The Hall bar was etched such that there was a 20% over etch to make sure all BN was removed from outside the Hall bar. The sample was annealed at 1600°C for 1 hour in a closed crucible. A typical AFM Hall bar at this step is shown in fig 36. This particular image was taken with NC-AFM overnight. FLG legs were etched using MaN and the hBN as a mask. Finally, Pd/Au was deposited on the FLG, and the sample was wire bonded. The total process flow is shown in fig 36.

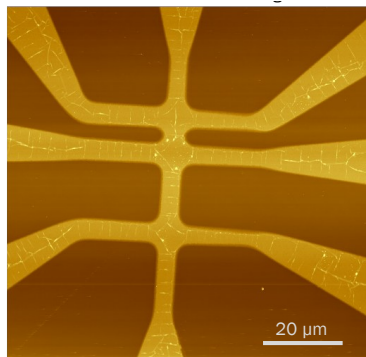


*fig 36 AFM image of a typical Hall bar with 9.5 and 20 μm legs*

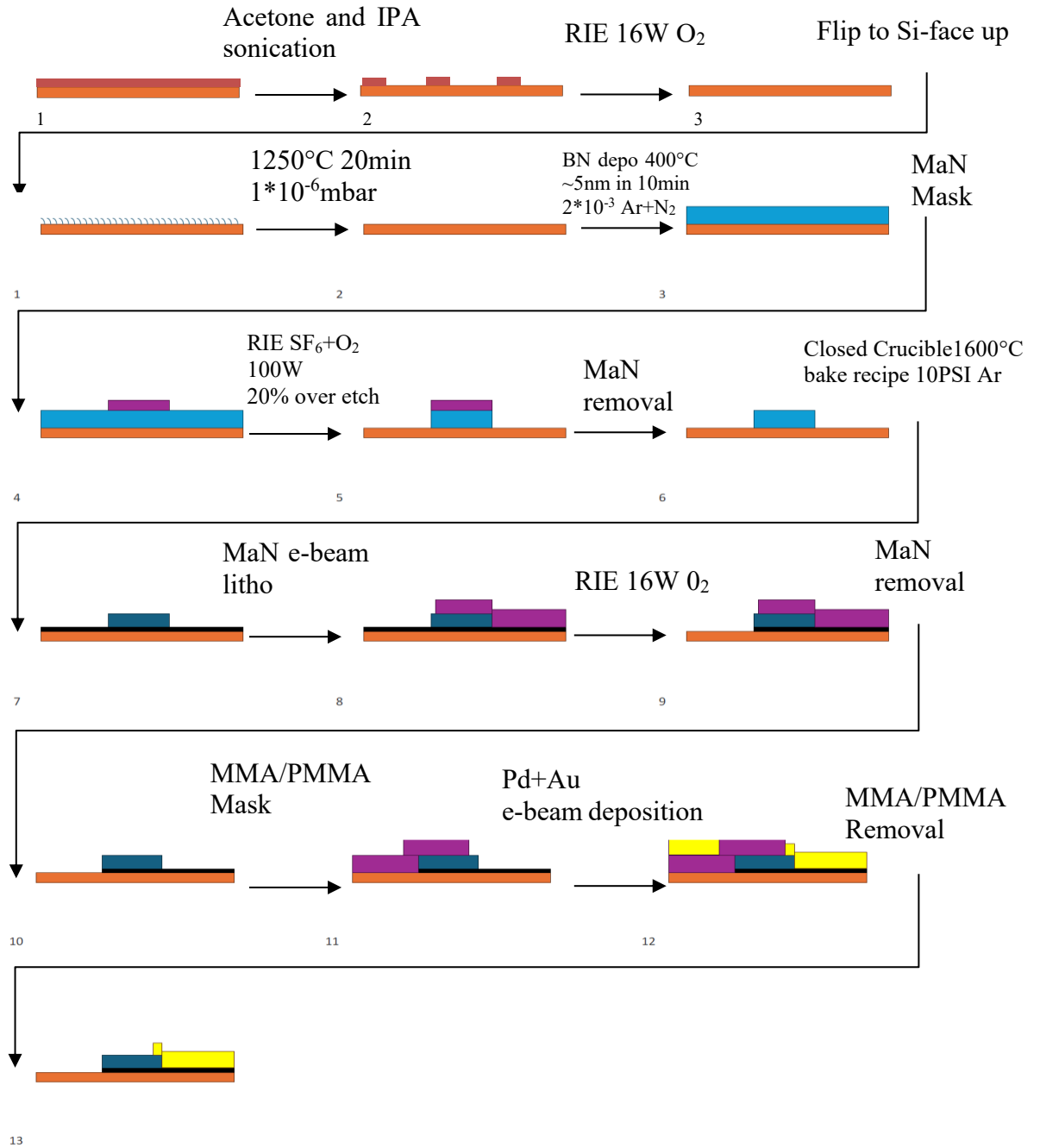


fig 37 Process flow for Hall bar sample. Orange: SiC, Black: EG or FLG, Blue: BN, Dark Blue: hBN, Yellow: Pd/Au Purple: Mask Red: Glue

## 4.2 Low Temperature Transport

Current was injected from the top to bottom according to fig 23 and the four-point resistance was measured at various temperatures. The charge density was measured using the Hall bar and was found to be  $n \approx 2.3 \times 10^{12} \text{cm}^{-2}$  at 4.2K where fig 38 right shows the charge density at all temperatures measured and fig 38 left is the mobility at those same temperatures. This charge density is about the same as monolayer epigraphene on the Si-face in UHV previously showing the graphene is well protected.

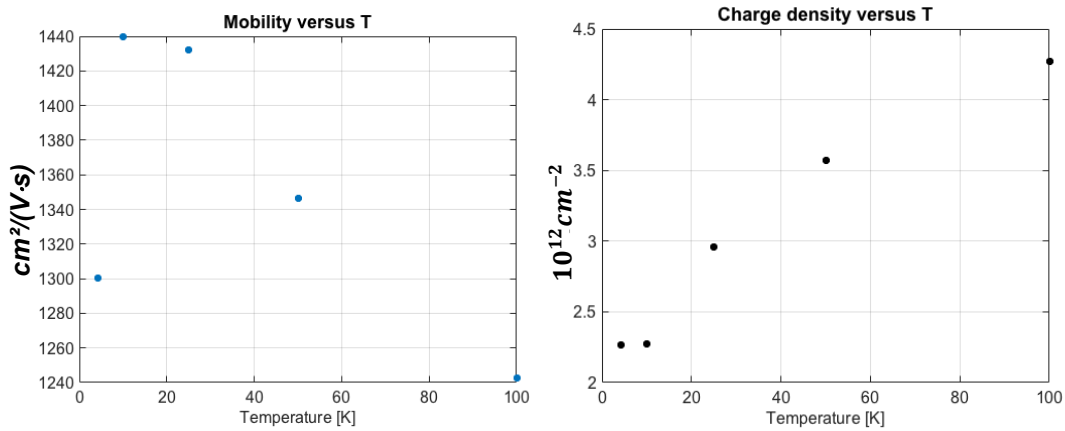


fig 38 Mobility and charge density as a function of temperature.

All measurements made are 4-point measurements except for the 2-point measurement described in 2.8. The measured resistance is shown in fig 39 and the Hall resistance is shown in fig 40 b . Upon measuring the 10  $\mu\text{m}$  (actually 9.5) and 20  $\mu\text{m}$  length arms, we see that the resistance does not scale linearly with the length. Shown in fig 39 is the cleanest data, for the 9.5  $\mu\text{m}$  length of the Hall bar as it had less noise, but it made no difference which side of the Hall bar we used. Correcting for the size by looking at the square resistance reveals that the 9.5 $\mu\text{m}$  leg has significant higher square resistance, which is unexpected and shown in fig 40 a. Using our previous knowledge, we can choose to separate the measured resistance into two resistors in parallel.

$$\frac{1}{R_{L,measured}(T)} = \frac{1}{R_{L,Bulk}(T)} + \frac{1}{R_{L,Edge}(T)} \quad (14)$$

where L denotes which length segment we are referring to and bulk and the edge resistance are defined as,

$$R_{L,Bulk}(T) = \frac{\rho_{L,Bulk}(T)L}{w} \quad (15)$$

$$R_{L,Edge}(T) = \frac{1}{G_{edge}(T)} = \frac{1}{G_0(T)T_n} \quad (16)$$

where  $T_n$  is the transmission coefficient

$$T_n = \left(1 + \frac{L}{\lambda}\right)^{-1} \quad (17)$$

Assuming there is a diffusive channel of conduction made up of many states with a low mfp and one ballistic channel with a mfp much greater than the bulk, we solve just for the diffusive part with a ballistic transport resistance of  $R_0$ , we obtain fig 41 left. We see that our estimated bulk square resistances become nearly equal at low temperature.

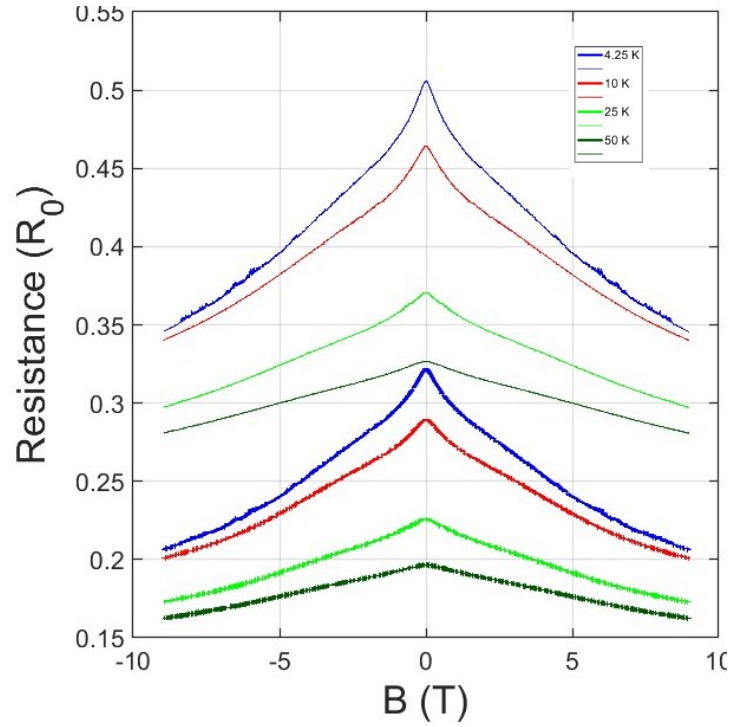


fig 39 Resistance of 9.5 and 20  $\mu\text{m}$  legs thin lines are 20  $\mu\text{m}$  thick line are 9.5  $\mu\text{m}$

This leads us to suspect the conductance of the edge is changing with temperature.

We observe that at 4.2K the resistivities of the bulk are equal for both lengths when we assume a single ballistic channel with  $T_n = 1$ .

$$\frac{\left(\frac{1}{R_{9.5,measured}} - \frac{1}{R_0}\right)w}{9.5\mu\text{m}} = \frac{\left(\frac{1}{R_{20,measured}} - \frac{1}{R_0}\right)w}{20\mu\text{m}} \quad (18)$$

We expect that our graphene is homogenous across the Hall bar at all temperatures

$$\frac{1}{\rho_{9.5,Bulk}} \cong \frac{1}{\rho_{20,Bulk}} \quad (19)$$

$\rho_{\text{diffusive}9.5}$  and  $\rho_{\text{diffusive}20}$  are the 9.5 and 20 $\mu\text{m}$  leg, respectively.

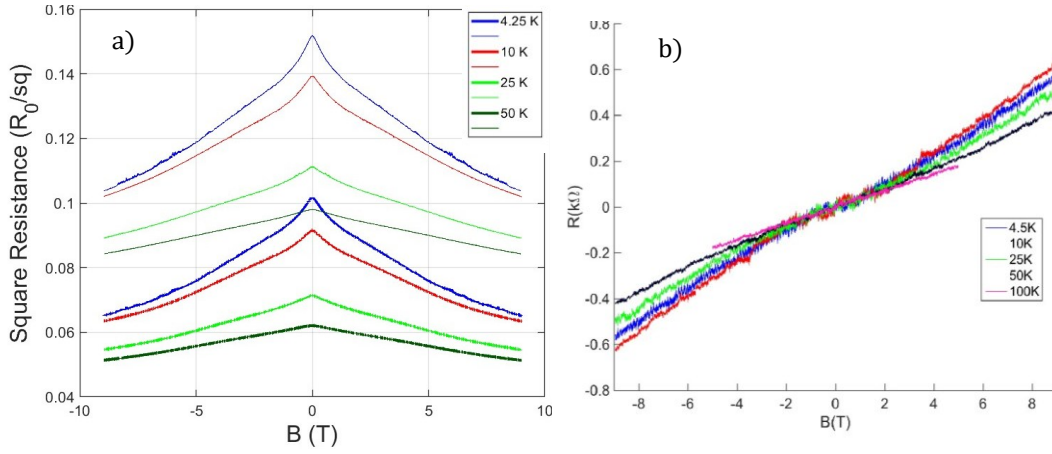


fig 40 Square resistance and Hall results a) Square Resistance of various temperatures and Hall resistance as a function of magnetic field b) Symmetrized Hall effect at different temperatures thin lines are 20  $\mu\text{m}$  thick lines are 9.5  $\mu\text{m}$

In fig 41 left, we see at low temperature the simple model of a single ballistic channel fits well; however, at higher temperatures, the difference between the estimated diffusive square resistance of the 9.5 and 20  $\mu\text{m}$  legs begin to differ. This effect is well explained by the splitting of the flat band at the edge between 2 spin states as shown in fig 5.

If we continue and use the Landauer equation instead of assuming infinite mfp of the diffusive part we can estimate the edge state conductance of our sample.

$$f_{\text{min}W} = \frac{1}{\rho_{9.5,\text{Bulk}}} - \frac{1}{\rho_{20,\text{Bulk}}} \quad (20)$$

$$f_{\min}(G_{edge}, \lambda) = \left( \frac{1}{R_{9.5,measured}} - \frac{G_{edge}}{1 + \frac{9.5\mu m}{\lambda}} \right) * 9.5\mu m - \left( \frac{1}{R_{20,measured}} - \frac{G_{edge}}{1 + \frac{20\mu m}{\lambda}} \right) * 20\mu m \quad (21)$$

setting the mfp,  $\lambda$ , to infinity gives:

$$f_{\min}(G_{edge}, \infty) = g_{\min}(G_{edge}) \quad (22)$$

$$g_{\min}(G_{edge}) = \left( \frac{1}{R_{9.5,measured}} - G_{edge} \right) * 9.5\mu m - \left( \frac{1}{R_{20,measured}} - G_{edge} \right) * 20\mu m \quad (23)$$

We can then minimize  $g_{\min}(G_{edge})$  and fit  $G_{edge}$  to obtain fig 42.

If we use  $f_{\min}(G_{edge}, \lambda)$  and fit  $G_{edge}$  and  $\lambda$  we obtain fig 41 right and fig 43 left for the mfp of the edge state. Because  $\lambda$  is over 100 times the length of this sample, these mfp numbers are not as accurate as they could be. Large changes in  $\lambda$  will lead to small changes in the fit, so we calculate  $\lambda = 1080 \mu m \pm 228 \mu m$  (1 standard deviation).

The result of the fit gives a mfp increase with temperature. This is unexpected as normally an increase in temperature will lead to a decrease in the mfp as electrons have a higher probability of transitioning to a new state. This increase is related to the second edge state.

There is a clear peak at zero field that is unrelated to the bulk as it does not scale with length. It might be related to edge state, but the mechanism is not understood.

We know that the edge state resistance has a peak. The fact that this peak does not scale with length means that it is not related to the bulk. So we can isolate this extra edge interaction by taking the two conductances and subtracting them from each other, assuming we scaled the lengths correctly.

$$G_{edgetotal} = G_{edgedip} + G_{edge} \quad (24)$$

Where

$$f_{\min}(G_{edge}, \gamma) = G_{edgedip} \quad (25)$$

And  $G_{edge}$  is a constant.

At high fields the assumption that conductivity equals the inverse of resistivity fails. So looking at zero field, we can plot the dip amplitude as a function of temperature to obtain fig 43 right.

The Hall measurements are most likely shorted by the edge state. However, since the legs of the Hall bar do not share the same ZZ edge direction as the body of the Hall bar and have a more complicated geometry, it is unclear what the bulk measurements would be.

This experiment can be improved on. Since this sample does not have a gate, we were unable to completely suppress the bulk states by lowering the Fermi level such that

there is no more contribution from the bulk states. Furthermore, the mfp of the edge state is much larger than our sample size. Therefore, it would be interesting to have a sample about the size of the mfp. We seek to improve this experiment by two methods. The first is to make a Hall bar the same size as our observed mfp  $\sim 1$  mm and we wish to add a gate to the sample to adjust the zero-energy edge state to lie between the band gap of the bulk.

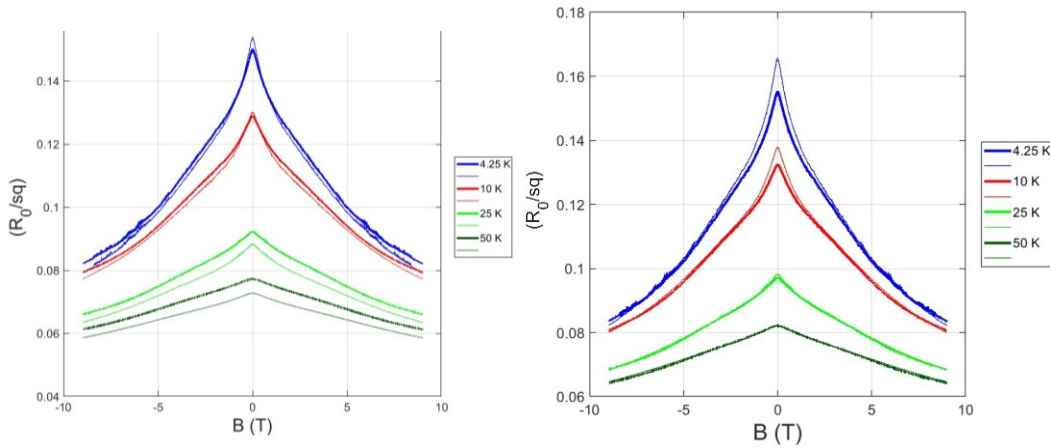


fig 41 Bulk square resistance adjusted left) Square resistance with the ballistic portion removed assuming mfp goes to infinity  $G_{edge} = 1.06$  right) Bulk square resistance after minimizing  $f_{min}$  thin lines are 20  $\mu m$  thick lines are 9.5  $\mu m$ .

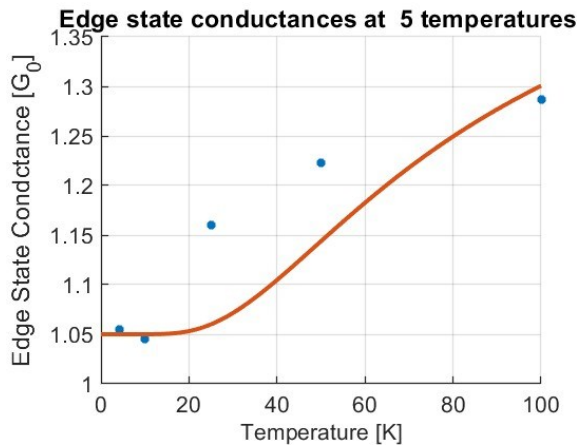


fig 42 Edge state conductance with a Fermi-Dirac distribution fit of 2 states with one state being 10meV above the Fermi energy and the other at the Fermi energy

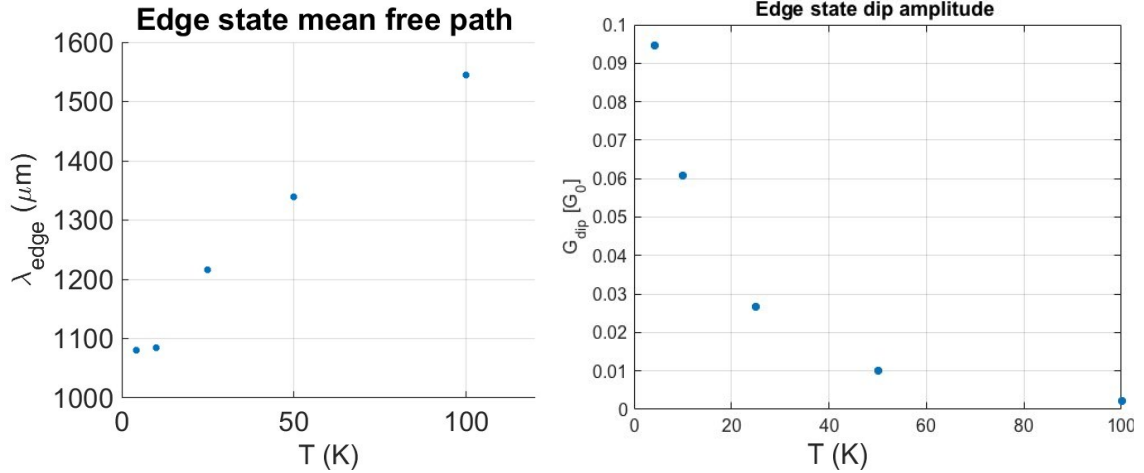


fig 43 Edge state results left)mfp after minimizing fmin right)Edge state dip amplitude evaluated at  $B=0$

This large mean free path leads us to wonder what happens to the edge state at these extreme length scales. We can estimate the mfp from the Landauer equation to be greater than 1 mm in length. Compared to ballistic transport in EG nanoribbon which have mfps on the order of tens of  $\mu\text{ms}$ , hBN preserves the edge state from the environment.

This method relies on a few assumptions, that can be solved in future experiments. We assume we can separate the edge state and the bulk state. In previous EG samples, we have shown the bulk and edge states do not mix; however, we are not able to show that in this sample since there is no gate. Furthermore, since the calculated mfp is much more than our sample length, a sample with legs on the order of the mfp will better show ballistic contributions. In addition, since the contribution from the bulk depends on the number of states available, we can add a gate and remove the contribution from the bulk leaving only the edge state.

## CHAPTER 5. CONCLUSION

I have presented data and analysis showing an edge state  $G_{edge} = 1.068 \pm 0.005$  with a mfp much larger than the length of the sample,  $\lambda = 1080 \mu m \pm 228 \mu m$  at 4.2K. The edge state consists of a single state at low temperature and as we increase the temperature, the second edge state begins to appear as some electrons have enough thermal energy to access it. The separation between these states is estimated to be 10meV. More devices are possible, and more research is needed to determine the exact nature of the edge state.

A process to easily make a gate on hBN was being worked on where PTCDA was deposited on hBN such that Alumina could be deposited on top. Such a method will be invaluable for all hBN/EG devices as we can come closer to the charge neutrality point with a gate.

A sample with legs on the order of the mfp would be the final test to ballistic conduction. Such a device holds some challenges. Long structures on the order of millimeters with a small width on the order of 250 nm is possible with modern e-beam lithography available at the Marcus Cleanroom. With a high bulk resistance, which is much greater than  $R_0$ , we can expect to see evidence of the edge state without a gate and have a more precise measurement of the mfp. A much longer Hall bar would allow us to confirm the mfp of the edge state so that equation 21 can give a precise value for the mfp. Such a large device has its own challenges. A device on that large of a scale must have graphene which is homogenous across a large area. This is possible, but not trivial. Precise design

and manufacturing of the crucible and large induction coils will be a must to achieve the most consistent graphene growth on a single 1 mm terrace. Furthermore, characterization will also present challenges. AFM measurements of the surface across such a large area will be time consuming and Raman measurements would also take a while, but can be more easily automated.

There are other device structures that would be interesting with this heterostructure. A Hall bar with asymmetric legs would test exactly where the edge state exists. When a probe is placed on one side of the Hall bar, how does that affect the edge state? Does manipulating one side of the edge affect the other side? Such a device might look like fig 44 left.

We would expect a single probe to still create a scattering center. Theory supports this idea[21]. However, from a classical perspective, it is counter intuitive. Since there are two sides of the Hall bar, it would make sense that there would be two states, top and bottom. However, we observe only one state, and only at high temperature do we see a second state. If we observe ballistic transport in both the left and right side of the Hall bar, this would be a novel example of non-locality, where affecting one side of the Hall bar affects the entire edge state.

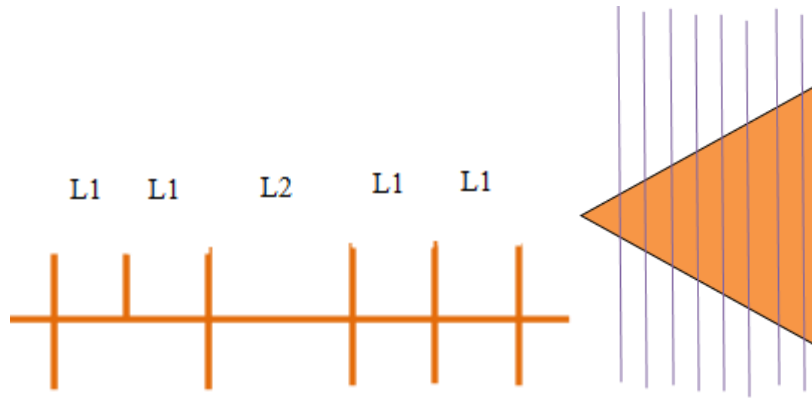


*fig 44 Potential Devices Left) Asymmetric Hall bar schematic. Right) 60-degree Hall bar*

Another novel device would be a 60-degree Hall bar shown in fig 44 right. 60 degrees is chosen such that the edges of the graphene remain with the same orientation. Current would be injected at the tip of the triangle where edges angled at 60 degrees would diverge away from each other. 4-point measurements would be made with a gate, where we can observe the resistivity of the edge as a function of distance between the edges. Is there some critical length where the edge state disappears? Finally, we would like to observe if the edge state is preserved after a 120-degree angle. Perhaps, the angle acts as an invasive contact, or perhaps nothing happens at all.

If the edge state persists throughout the triangular Hall bar, we show that the edge state is independent of the width of the Hall bar. Namely, the two sides of the edge state do not need to be parallel. The edge state may degrade and the mfp may decrease. These are some of the questions we hope to answer with this device.

These new devices will give a more complete picture of the edge state of EG. If the making of gates on BN can be perfected and a larger device is made, we can confirm that the mfp is on the order of mms. This is the beginning of what the edge state has to offer, and hopefully future researchers can discover the rest.

## REFERENCES

1. Geim, A.K. and K.S. Novoselov, *The rise of graphene*. Nature Materials, 2007. **6**(3): p. 183.
2. Novoselov, K.S., et al., *Two-dimensional gas of massless Dirac fermions in graphene*. Nature, 2005. **438**(7065): p. 197.
3. Edelstein, V.M., *spin polarization of conduction electrons induced by electric current in two dimensional asymmetric electron systems*. Solid State Communications, 1990. **73**: p. 233-235.
4. Beenakker, C.W.J. and H. Vanhouten, *Quantum Transport in Semiconductor Nanostructures*. Solid State Physics-Advances in Research and Applications, 1991. **44**: p. 1-228.
5. Gall, N.R., E.V. RutKov, and A.Y. Tontegode, *Two dimensional graphite films on metals and their intercalation*. International Journal of Modern Physics B, 1997. **11**(16): p. 1865-1911.
6. Ugarte, D., et al., *Filling carbon nanotubes*. Applied Physics A-Materials Science & Processing, 1998. **67**(1): p. 101.
7. Zheng, Y.S. and T. Ando, *Hall conductivity of a two-dimensional graphite system*. Physical Review B, 2002. **65**(24).
8. Yi, C.W., et al., *Evidence of Plasmonic Coupling in Gallium Nanoparticles/Graphene/SiC*. Small, 2012. **8**(17): p. 2721-2730.
9. Castro Neto, A.H., et al., *The electronic properties of graphene*. Reviews of Modern Physics, 2009. **81**(1): p. 109-162.
10. Palacio, I., et al., *Atomic Structure of Epitaxial Graphene Sidewall Nanoribbons: Flat Graphene, Miniribbons, and the Confinement Gap*. Nano Letters, 2015. **15**: p. 182–189.
11. Griffiths, D.J. and D.F. Schroeter, *Introduction to Quantum Mechanics*. 3rd ed. 2018, Cambridge: Cambridge University Press.
12. Avouris, P. and F.N. Xia, *Graphene applications in electronics and photonics*. MRS Bulletin, 2012. **37**(12): p. 1225-1234.
13. Berger, C., E. Conrad, and W.A. de Heer, *Epigraphene*, in *Physics of Solid Surfaces, Landolt Börstein encyclopedia* P.C. G. Chiarotti, Editor. 2018, Springer-Verlag: Germany. p. 727-807. ArXiv:1704.00374.

14. Berger, C., et al., *High Mobility Epitaxial Graphene for Carbon-based Nanoelectronics*, in *ECS transactions – ULSI Process Integration 7*. 2011. p. 43-55.
15. Baringhaus, J., et al., *Exceptional ballistic transport in epitaxial graphene nanoribbons*. *Nature*, 2014. **506**(7488): p. 349-354.
16. Novoselov, K.S., et al., *Two-dimensional atomic crystals*. *Proceedings of the National Academy of Sciences of the United States of America*, 2005. **102**(30): p. 10451-10453.
17. Wang, X.R. and H.J. Dai, *Etching and narrowing of graphene from the edges*. *Nature Chemistry*, 2010. **2**(8): p. 661-665.
18. Hibino, H., et al., *Growth and electronic transport properties of epitaxial graphene on SiC*. *Journal of Physics D-Applied Physics*, 2012. **45**(15): p. 154008.
19. Michon, A., et al., *Effects of pressure, temperature, and hydrogen during graphene growth on SiC(0001) using propane-hydrogen chemical vapor deposition*. *Journal of Applied Physics*, 2013. **113**(20): p. 203501.
20. Roth, S., et al., *Chemical Vapor Deposition and Characterization of Aligned and Incommensurate Graphene/Hexagonal Boron Nitride Heterostack on Cu(111)*. *Nano Letters*, 2013. **13**(6): p. 2668-2675.
21. Datta, S., *Electronic Transport in Mesoscopic Systems*. *Cambridge Studies in Semiconductor Physics and Microelectronic Engineering*. 1995, Cambridge: Cambridge University Press.
22. Ashcroft, N.W. and N.D. Mermin, *Solid State Physics*. Holt-Saunders, 1976.
23. Ferralis, N., R. Maboudian, and C. Carraro, *Evidence of Structural Strain in Epitaxial Graphene Layers on 6H-SiC(0001)*. *Physical Review Letters*, 2008. **101**(15).
24. Park, C.H., et al., *First-Principles Study of Electron Linewidths in Graphene*. *Physical Review Letters*, 2009. **102**(7): p. 189904.
25. Schwierz, F., *Graphene transistors*. *Nature Nanotechnology*, 2010. **5**(7): p. 487-496.
26. Sprinkle, M., et al., *Scalable templated growth of graphene nanoribbons on SiC*. *Nature Nanotechnology*, 2010. **5**(10): p. 727-731.
27. Bonaccorso, F., et al., *Graphene photonics and optoelectronics*. *Nature Photonics*, 2010. **4**(9): p. 611-622.

28. Balog, R., et al., *Bandgap opening in graphene induced by patterned hydrogen adsorption*. Nature Materials, 2010. **9**(4): p. 315-319.
29. Hertel, S., et al., *Tailoring the graphene/silicon carbide interface for monolithic wafer-scale electronics*. Nature Communications, 2012. **3**: p. 957.
30. Moon, J.S., et al., *Lateral Graphene Heterostructure Field-Effect Transistor*. IEEE Electron Device Letters, 2013. **34**(9): p. 1190-1192.
31. Xia, F.N., H.G. Yan, and P. Avouris, *The Interaction of Light and Graphene: Basics, Devices, and Applications*. Proceedings of the Ieee, 2013. **101**(7): p. 1717-1731.
32. Mihnev, M.T., et al., *Evidence for bandgap opening in buckled epitaxial graphene from ultrafast time-resolved terahertz spectroscopy*. Applied Physics Letters, 2015. **107**(17): p. 173107(5pp).
33. Geng, D., et al., *In Situ Epitaxial Engineering of Graphene and h-BN Lateral Heterostructure With a Tunable Morphology Comprising h-BN Domains*. NPG Asia Materials, 2019. **11**(1): p. 56.
34. Prudkovskiy, V., et al., *An epitaxial graphene platform for zero-energy edge state nanoelectronics*. Nature Communications, 2022.
35. Brey, L., P. Seneor, and A. Tejeda, *Graphene Nanoribbons*. 2019: IOP Publishing.
36. Datta, S., F. Assad, and M.S. Lundstrom, *The silicon MOSFET from a transmission viewpoint*. Superlattices and Microstructures, 1998. **23**(3-4): p. 771-780.
37. Hu, Y., *The Edge States of Epitaxial Graphene on SiC*, in *School of Physics*. 2021, Georgia Institute of Technology: Atlanta, GA, USA.
38. Plasser, F., et al., *The Multiradical Character of One- and Two-Dimensional Graphene Nanoribbons*. Angewandte Chemie-International Edition, 2013. **52**(9): p. 2581-2584.
39. Desjardins, M.M., et al., *Synthetic spin-orbit interaction for Majorana devices*. Nature Materials, 2019. **on line**: p. Aug.
40. Ji, W.J. and X.G. Wen, *1/2 (e<sup>2</sup>/h) Conductance Plateau without 1D Chiral Majorana Fermions*. Physical Review Letters, 2018. **120**(10): p. 107002.
41. San-Jose, P., et al., *Majorana Zero Modes in Graphene*. Physical Review X, 2015. **5**(4): p. 041042.
42. Majorana, E., *Teoria simmetrica dell'elettrone e del positrone*. Il Nuovo Cimento, 1937. **14**: p. 171-184.

43. Brodie, B.C., *On the Atomic Weight of Graphite*. Royal Society, 1859. **149**: p. 249-259.
44. Geim, A.K., *Graphene prehistory*. Physica Scripta, 2012. **2012**(T146): p. 014003.
45. Dreyer, D.R., et al., *The chemistry of graphene oxide*. Chemical Society Reviews, 2010(1460-4744 (Electronic)).
46. Ruess, G. and F. Vogt, *Höchstlamellarer Kohlenstoff aus Graphitoxhydroxyd*. Monatshefte für Chemie, 1948. **78**(3): p. 222-242.
47. Boehm, H.P., et al., *Surface properties of extremely thin graphite lamellae*. Proceeding of the 5th conference on Carbon, 1962: p. 73-80.
48. Boehm, H.P., et al., *Dunnste Kohlenstoff-Folien*. Zeitschrift Fur Naturforschung Part B-Chemie Biochemie Biophysik Biologie Und Verwandten Gebiete, 1962. **B 17**(3): p. 150-153.
49. Wallace, P.R., *The Band Theory of Graphite*. Physical Review, 1947. **71**(9): p. 622-634.
50. Berger, C., et al., *Ballistic conduction in multiwalled carbon nanotubes*. Journal of Nanoscience and Nanotechnology, 2003. **3**(1-2): p. 171-177.
51. Chung, D.D.L., *Review graphite*. Journal of Materials Science, 2002. **37**(8): p. 1475-1489.
52. Novoselov, K.S., et al., *A roadmap for graphene*. Nature, 2012. **490**(7419): p. 192-200.
53. Liao, L., et al., *Scalable Fabrication of Self-Aligned Graphene Transistors and Circuits on Glass*. Nano Letters, 2012. **12**(6): p. 2653-2657.
54. Hummers, W.S. and R.E. Offeman, *Preparation of Graphitic Oxide*. Journal of the American Chemical Society, 1958. **80**(6): p. 1339-1339.
55. Marcano, D.C., et al., *Improved Synthesis of Graphene Oxide*. ACS Nano, 2010. **4**(8): p. 4806-4814.
56. Wei, Z., et al., *Nanoscale Tunable Reduction of Graphene Oxide for Graphene Electronics*. Science, 2010. **328**(5984): p. 1373-1376.
57. Nakada, K., et al., *Edge state in graphene ribbons: Nanometer size effect and edge shape dependence*. Physical Review B, 1996. **54**(24): p. 17954-17961.
58. Ryu, S. and Y. Hatsugai, *Topological Origin of Zero-Energy Edge States in Particle-Hole Symmetric Systems*. Physical Review Letters, 2002. **89**(7): p. 077002.

59. Kane, C.L. and E.J. Mele, *Quantum spin Hall effect in graphene*. Physical Review Letters, 2005. **95**(22): p. 226801.
60. Son, Y.W., M.L. Cohen, and S.G. Louie, *Energy gaps in graphene nanoribbons*. Physical Review Letters, 2006. **97**(21): p. 216803.
61. Kobayashi, Y., et al., *Edge state on hydrogen-terminated graphite edges investigated by scanning tunneling microscopy*. Physical Review B, 2006. **73**(12): p. 125415.
62. Abanin, D.A., P.A. Lee, and L.S. Levitov, *Spin-filtered edge states and quantum hall effect in graphene*. Physical Review Letters, 2006. **96**(17).
63. Brey, L. and H.A. Fertig, *Edge states and the quantized Hall effect in graphene*. Physical Review B, 2006. **73**(19): p. 195408.
64. Takahashi, T., et al., *Band-gap tuning of monolayer graphene by oxygen adsorption*. Carbon, 2014. **73**: p. 141-145.
65. Hu, Y., *Graphene on non-polar SiC facets*, in *School of Physics*. 2020, Georgia Institute of Technology: Atlanta, GA, USA.
66. de Heer, W.A., C. Berger, and P.N. First, *Patterned thin films graphite devices and methods for making the same*. US patent US7015142B2 (Provisional filed Jun. 12, 2003; granted March 3, 2006); European patent EP1636829B. This patent, based on experimental evidence, includes a detailed description of practical epitaxial graphene coherent nanoelectronics.
67. *Silicon carbide (SiC), polytypes: Datasheet from Landolt-Börnstein - Group III Condensed Matter · Volume 41A1β: "Group IV Elements, IV-IV and III-V Compounds. Part b - Electronic, Transport, Optical and Other Properties" in SpringerMaterials ([http://dx.doi.org/10.1007/10832182\\_594](http://dx.doi.org/10.1007/10832182_594)), O. Madelung, U. Rössler, and M. Schulz, Editors., Springer-Verlag Berlin Heidelberg.*
68. Beattie, J.M.A., et al., *Structure and electron affinity of the 4H-SiC (0001) surfaces: a methodological approach for polar systems*. Journal of Physics: Condensed Matter, 2021. **33**(16): p. 165003.
69. Casady, J.B. and R.W. Johnson, *Status of silicon carbide (SiC) as a wide-bandgap semiconductor for high-temperature applications: A review*. Solid-State Electronics, 1996. **39**(10): p. 1409-1422.
70. Renbing Wu, K.Z., Chee Yoon Yue, Jun Wei, Yi Pan, *Recent progress in synthesis, properties and potential applications of SiC nanomaterials*. Progress in Materials Science, 2015. **72**.
71. Prudkovskiy, V.S., et al., *Local potentiometry and ballistic transport in epigraphene nanoribbons*. unpublished, 2018.

72. Syväjärvi, M., R. Yakimova, and E. Janzén, *Step-bunching in SiC epitaxy: anisotropy and influence of growth temperature*. Journal of Crystal Growth, 2002. **236**(1): p. 297-304.
73. Kimoto, T., *Bulk and epitaxial growth of silicon carbide*. Progress in Crystal Growth and Characterization of Materials, 2016. **62**(2): p. 329-351.
74. Berger, C., et al., *Electronic confinement and coherence in patterned epitaxial graphene*. Science, 2006. **312**(5777): p. 1191-1196.
75. de Heer, W.A., et al., *Epitaxial graphene electronic structure and transport*. Journal of Physics D: Applied Physics, 2010. **43**(37): p. 374007.
76. Kruskopf, M., et al., *Epitaxial graphene on SiC: modification of structural and electron transport properties by substrate pretreatment*. Journal of Physics-Condensed Matter, 2015. **27**(18).
77. Shi, Y.C., et al., *Elimination of step bunching in the growth of large-area monolayer and multilayer graphene on off-axis 3C-SiC (111)*. Carbon, 2018. **140**: p. 533-542.
78. Xian, L. and M.Y. Chou, *Diffusion of Si and C atoms on and between graphene layers*. Journal of Physics D: Applied Physics, 2012. **45**(45): p. 455309.
79. Forbeaux, I., J.M. Themlin, and J.M. Debever, *Heteroepitaxial graphite on 6H-SiC(0001): Interface formation through conduction-band electronic structure*. Physical Review B, 1998. **58**(24): p. 16396-16406.
80. Berger, C., et al., *Ultrathin Epitaxial Graphite: 2D Electron Gas Properties And a Route Toward Graphene-Based Nanoelectronics*. Journal of Physical Chemistry B, 2004. **108**(52): p. 19912-19916.
81. Johansson, L.I., et al., *Multiple  $\pi$ -bands and Bernal stacking of multilayer graphene on C-face SiC, revealed by nano-Angle Resolved Photoemission*. Scientific Reports, 2014. **4**(1): p. 4157.
82. Hass, J., et al., *Highly ordered graphene for two dimensional electronics*. Applied Physics Letters, 2006. **89**(14): p. 143106.
83. Ristein, J., S. Mammadov, and T. Seyller, *Origin of Doping in Quasi-Free-Standing Graphene on Silicon Carbide*. Physical Review Letters, 2012. **108**(24).
84. First, P.N., et al., *Epitaxial Graphenes on Silicon Carbide*. MRS Bulletin, 2010. **35**(4): p. 296-305.
85. Daas, B.K., et al., *Comparison of Epitaxial Graphene Growth on Polar and Nonpolar 6H-SiC Faces: On the Growth of Multilayer Films*. Crystal Growth & Design, 2012. **12**(7): p. 3379-3387.

86. Gigliotti, J., et al., *Highly Ordered Boron Nitride/Epigraphene Epitaxial Films on Silicon Carbide by Lateral Epitaxial Deposition*. ACS Nano, 2020. **14**(10): p. 12962-12971.
87. Sun, X., et al., *Correlated states in doubly-aligned hBN/graphene/hBN heterostructures*. Nature Communications, 2021. **12**(1): p. 7196.
88. Kim, S.M., et al., *Synthesis of Patched or Stacked Graphene and hBN Flakes: A Route to Hybrid Structure Discovery*. Nano Letters, 2013. **13**(3): p. 933-941.
89. Cho, Y.-J., et al., *Hexagonal Boron Nitride Tunnel Barriers Grown on Graphite by High Temperature Molecular Beam Epitaxy*. Scientific Reports, 2016. **6**(1): p. 34474.
90. Epping, A., et al., *Insulating State in Low-Disorder Graphene Nanoribbons*. physica status solidi (b), 2019. **256**(12): p. 1900269.
91. Ansari, N., F. Nazari, and F. Illas, *Line defects and induced doping effects in graphene, hexagonal boron nitride and hybrid BNC*. Phys. Chem. Chem. Phys., 2014. **16**(39): p. 21473-21485.
92. Bistrizter, R. and A.H. MacDonald, *Moiré bands in twisted double layer graphene*. Proc Natl Acad Sci, 2011. **108**(30): p. 12233-12237.
93. Xue, J., et al., *Scanning tunnelling microscopy and spectroscopy of ultra-flat graphene on hexagonal boron nitride*. Nature Materials, 2011. **10**(4): p. 282-285.
94. Chatterjee, A., et al., *Impact of Polymer-Assisted Epitaxial Graphene Growth on Various Types of SiC Substrates*. ACS Applied Electronic Materials, 2022. **4**(11): p. 5317-5325.
95. *Negative Photoresist*. [cited 2024 12/30/2024]; Available from: <https://www.microchemicals.com/PRODUCTS/Photochemicals/Photoresist/Negative-Resist/>.
96. Mieno, M. and T. Yoshida, *Preparation of Cubic Boron Nitride Films by RF Sputtering*. Japanese Journal of Applied Physics, 1990. **29**(7A): p. L1175.
97. Narayan, J. and A. Bhaumik, *Research Update: Direct conversion of h-BN into pure c-BN at ambient temperatures and pressures in air*. APL Materials, 2016. **4**: p. 020701.
98. Wang, G., et al., *Epitaxy of Hexagonal Boron Nitride Thin Films on Sapphire for Optoelectronics*. Crystal Growth & Design, 2022. **22**(12): p. 7207-7214.
99. Zedlitz, R., M. Heintze, and M.B. Schubert, *Properties of amorphous boron nitride thin films*. Proceedings of the Sixteenth International Conference on Amorphous Semiconductors - Science and Technology, 1996. **198-200**: p. 403-406.

100. Tuinstra, F. and J.L. Koenig, *Raman Spectrum of Graphite*. Journal of Chemical Physics, 1970. **53**(3): p. 1126-&.
101. Ferrari, A.C., et al., *Raman Spectrum of Graphene and Graphene Layers*. Physical Review Letters, 2006. **97**(18).
102. Ferrari, A.C., *Raman spectroscopy of graphene and graphite: Disorder, electron-phonon coupling, doping and nonadiabatic effects*. Solid State Communications, 2007. **143**(1-2): p. 47-57.
103. Ferrari, A.C. and D.M. Basko, *Raman spectroscopy as a versatile tool for studying the properties of graphene*. Nature Nanotechnology, 2013. **8**(4): p. 235-246.
104. Hu, Z.P., et al., *LEED Theory for Incommensurate Overlayers - Application to Graphite on Pt(111)*. Surface Science, 1987. **180**(2-3): p. 433-459.
105. Guo, H., A.J. Martínez-Galera, and J.M. Gómez-Rodríguez, *Molecular properties of PTCDA on graphene grown on a rectangular symmetry substrate*. Applied Surface Science, 2023. **620**: p. 156777.
106. Huang, H., et al., *Structural and electronic properties of PTCDA thin films on epitaxial graphene*. ACS Nano, 2009. **3**(11): p. 3431-6.
107. Wang, Q.H. and M.C. Hersam, *Room-temperature molecular-resolution characterization of self-assembled organic monolayers on epitaxial graphene*. Nature Chemistry, 2009. **1**(3): p. 206-211.
108. *Digital lock-in amplifiers*. 2024 [cited 2024 December 27th, 2024]; Available from: <https://www.lakeshore.com/products/product-detail/m81/digital-lock-in-amplifier/>.
109. Gorbachev, R.V., et al., *Hunting for Monolayer Boron Nitride: Optical and Raman Signatures*. Small, 2011. **7**(4): p. 465-468.
110. Seah, M.P. and W.A. Dench, *Quantitative electron spectroscopy of surfaces: A standard data base for electron inelastic mean free paths in solids*. 1979. **1**(1): p. 2-11.
111. Pierret, A., et al., *Dielectric permittivity, conductivity and breakdown field of hexagonal boron nitride*. Materials Research Express, 2022. **9**(6): p. 065901.